Università degli studi di Padova
Department of Industrial Engineering

Master of Science in
Electrical Energy Engineering

Master's Degree Thesis

Analysis of motors for more electric aircraft

Supervisor: Prof. Nicola Bianchi
Department of Industrial Engineering

Candidate: Nicolò Paolo
1171756

Academic Year 2018/2019

There must be a better way to make the things we want, a way that doesn't spoil the sky, or the rain or the land

---

Sir Paul McCartney

Contents

Introduction

Man's greatest dream in history has always been to fly. Exploring the skies meant to explore the unknown and inventing the means to do so symbolized the peak of human evolution.
Leonardo da Vinci tried, the Wright brothers, two engineers, succeeded by flying the first motorized machine.
Since then, men have not only realized this dream, but they have implemented it more and more, to such an extend that planes are among the most common means of transportation. Here is now the need to make sure that this dream does not turn into the main cause of environmental pollution.
In this thesis, we will examine the operation of two electric motor possibilities to reduce the plane need of fossil fuels as much as possible, in order to decrease the level of pollution. In particular, the applications of these engines starts from the papers by A. Cavagnino and S. Shoujun and collaborators, mentioned in the bibliography.
The first chapter will focus on the description of the pollution problem and in particular the increase of the environmental impact of aviation. The second chapter will be dedicated to the comparison between the various traditional aircraft operating systems, the one operating today, and the "more electric " one that we are going to analyse. The third chapter will deal with the operation of the electric motor and its parameters. In the fourth chapter we will then examine the power losses of the motor with the relative dispersion of heat. Finally, we will illustrate the material possibilities for thermal insulation of the windings.

0.1 Italian version

Il sogno più grande dell'uomo nella storia è sempre stato quello di volare. Esplorare i cieli equivaleva ad esplorare l'ignoto ed inventare il mezzo per poterlo fare ha rappresentato il punto più elevato dell'evoluzione dell'uomo.
Leonardo da Vinci ci ha provato, i fratelli Wright, due ingegneri, ci riuscirono facendo volare con successo la prima macchina motorizzata.
Da allora, l'uomo non ha solo realizzato questo sogno, ma l'ha implementato sempre di più, tanto che oramai l'aereo è un mezzo di trasporto sempre più utilizzato e da qui nasce la necessità di far sì che il sogno non si traduca in una delle cause di inquinamento dell'ambiente.
In questo lavoro di tesi, pertanto, si cercherà di analizzare il funzionamento di due possibili motori elettrici per svincolare il più possibile l'aereo dai combustibili fossili, in modo da renderlo meno impattante sull'ambiente. In particolare, l'analisi di questi motori parte dagli articoli citati nella bibliografia di A. Cavagnino e S. Shoujun e collaboratori.
Verrà dedicato un primo capitolo alla descrizione del problema dell'inquinamento e in particolare di quello causato dall'intensificarsi del traffico aereo. Il secondo capitolo sarà dedicato alla comparazione tra i vari sistemi di funzionamento dell'aereo tradizionale, inteso quello operativo al giorno d'oggi, con quello "più elettrico" che andiamo ad analizzare. Il terzo capitolo affronterà l'effettivo funzionamento del motore elettrico ed i suoi parametri. Nel quarto capitolo si prenderà in esame le perdite di potenza del motore con la relativa dispersione di calore all'interno della macchina. Infine, si illustreranno i possibili materiali per l'isolamento termico degli avvolgimenti.

Chapter 1

Pollution and aircraft problem

Air pollution is a form of pollution, that is to say the set of physical, biological and chemical agents that modify the natural composition of the Earth's atmosphere. To define what pollution is, we must clarify the boundary between pollutant and non-pollutant. In 1973 Samuel J. Williamson proposed a distinction between pollutant and contaminant. He defines the contaminant as "everything that is added to the environment that causes a deviation from average geochemical composition"; the pollutant as a contaminant accountable to cause harmful effects to the environment.
Therefore, the air pollutant is a factor or a substance that determines an alteration of a stationary situation through the:

- Modification of physical, chemical and biological parameters.
- Variation of the quantitative ratio of substances already present.
- Direct or indirect input of harmful foreign compounds.

The foreign compounds can be divided between:

- Primary pollutants that are released directly into the atmosphere without any modification of their form. Carbon monoxide is an example of primary pollutant, as it is a by-product of the combustion. The particulate emitted by natural event can also be considered primary pollutants.

- Secondary pollutants are formed in the atmosphere whenever chemical reactions combine various substances present in the air (being them pollutants or not). An example of secondary pollutants is the formation of ozone from the smog.

Air pollution can be caused by:

- Natural sources: volcanoes (SO_2), fires (PM_{10}), etc.
- Human sources:

  1 **Vehicular traffic**; all cars release CO_2 but, depending on the type of vehicle, its age and fuel, they can release also other substances in different quantities. Diesel fuel releases particulate like PM_{10}, hydrocarbons (HC), nitrogen oxides (NO_x) and sulphur dioxides (SO_2); unleaded fuel releases particulate, nitrogen oxides and carbon monoxide (CO). Methane and GPL, on the other hand, release NO_x, ultra thin particulate and a small quantitative of hydrocarbons.

  2 **Home Heating**; the pollutants released are similar to the vehicular traffic ones and, except for carbon and wood, they all vary according to the same factors.

  3 **Craftsmanship and industry**; in this case the pollutants released are very different, because of all the various processing techniques.

1.1 Main pollutant

There are three main characteristics that identify all pollutants. They can be, therefore, classified according to: their chemical composition (sulphur, nitrogen, carbon or halogens compounds), their state of matter and their reactivity in the atmosphere.
Primary pollutants can be:

- **Gaseous**:

1 **Sulphur compounds**. The primary compounds are sulphur dioxides (SO_2), carbonyl sulphide (COS), carbon disulphide (CS_2), hydrogen sulphide (H_2S) and dimethyl sulphate $(CH_3)_2SO_4$. Their principal sources are the biological decomposition, fossil fuels and organic material combustion and volcanic eruptions.

   Sulphur dioxides make up 95% of the total anthropogenic sulphur emission.

   The trend of emission is decreasing for the home heating methanisation. Furthermore, these compounds remain in the atmosphere from 12 hours to 7 days, because they are very soluble in water. They, therefore, are removed from precipitation causing the vegetation and water basins contamination.

2 **Nitrogen compounds**. The main compounds are N_2O, NO, NO_2, NH_3, HNO_3, HONO, N_2O_5 and salts of NO_3, NO_2, NH_4. The N_2O is the most abundant in atmosphere. Even if it is released from the bacteria on the ground, it is not considered pollutant, as it is chemical inert at ordinary temperatures, although it is officially classified as greenhouse gas. On the other hand, nitrogen monoxide and dioxide (NO, NO_2) are pollutants. They are produced by combustion reactions at high temperatures. Nitrogen monoxide is produced more than the other one according to the combustion temperature and the oxygen percentage. Nitrogen dioxides are formed also through photochemical reactions thanks to ultraviolet radiations. They last about 4-5 days before being eliminated by chemical reactions that lead to the formation of acids and organic substances.

3 **Carbon compounds**. Carbon monoxide (CO) and carbon dioxide (CO_2) belongs to this category. The first one is considered highly toxic for humans as it prevents tissue oxygenation. The main cause of its formation is car exhaust gas (about 90%), but there are also natural emission like the methane or other hydrocarbons oxidation released by oceans and swamps, forest fires, etc. Carbon dioxide, too, is caused

mainly by human activities through combustion processes. In the past its level was balanced through the absorption by the green vegetation, now a sudden increase of its emission causes a growth of its concentration. The interest that is developed around it is due to the climate change on planetary scale. Today only few people ignore the meaning of climate change, at least compared to the standards of the last fifty years. The awareness of where we would end up began to take shape in unsuspected times, with a symbolic date: 1958. This is when Charles David Keeling, a geochemist from Pennsylvania, carried out the first survey on the carbon dioxide concentration from the top of the Mauna Loa, a 4,000 meters high volcano in the Hawaiian island. Keeling got there as a researcher at the Scripps Institution of Oceanography to record the levels of CO_2 in the atmosphere from the top of Mauna Loa. The results, 61 years later, are shown in black and white on the indicator named after him name, the "Keeling curve".

Figure 1.1: Keeling curve's trend until today. (Source: "Il Sole 24 Ore", 2019)

Apart from those carbon compounds, there are many others compounds arranged in different categories. The main ones are: hydrocarbons (subdivided into alkanes, as methane, into alkenes, as ethene, and into alkyne, as acetylene); aromatic compounds, as benzene; aldehydes, as formaldehyde; ketones.

4 **Halogens compounds**. This group in the periodic table consists of five chemically related elements: Fluorine, Chlorine, Bromine, Iodine and Astatine. All these atoms are very toxic and potentially letal for humans at very high concentration, but they tend to decrease in toxicity towards the heavier halogens.

5 **PAH**. They are organic compounds containing only hydrogen and carbon, and they are composed of multiple aromatic rings (organic rings in which the electrons are delocalized). They are powerful air pollutant, because some compounds have been identified as carcinogens, mutagens and teratogens; they develop for anthropic causes during incomplete combustion of fossil fuel, timber, foliage, incense and organic compounds in general (including from urban waste, biomass, tobacco smoke and cooked food, particularly in high temperature carbonization processes such as grilled meat or smoked fish).

- The **Particulate** is a microscopic suspended solid or liquid matter classified according to their diameter. They are divided into coarse particles (diameter between $2.5 - 10\mu m$, as PM_{10}) and fine particles (diameter of $2.5\mu m$ or less, as $PM_{2.5}$).The smaller ones are more dangerous, because they can penetrate further down the respiratory system. Nowadays, the attention is focusing on smaller particles, as $PM_{0.1}$, called ultra fine particles, which are considered more dangerous.

1.2 Effects of air pollution

In addition to the effects on human health, there are three environmental effects:

- **The stratospheric ozone depletion and hole**. These two phenomena are strictly connected to the ozone decrease, which means:

  1 a steady lowering of about four percent in the total amount of ozone in the Earth's atmosphere.

  2 a decreasing in stratospheric ozone around the Earth's polar regions (also known as the ozone hole).

  This decreasing can reach up to 71% on Antarctic region and 29% on Arctic one.

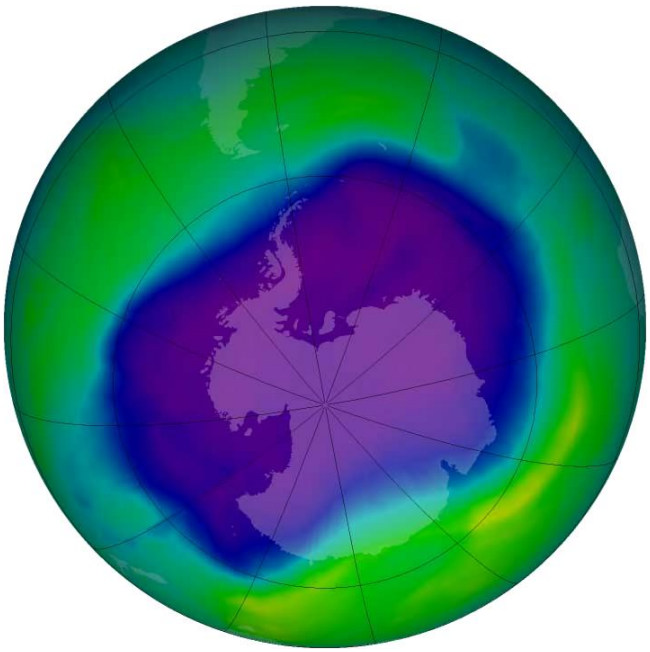

Figure 1.2: Antarctic region's ozone hole. (Source: "NASA", 2006)

The purple zone represents the ozone reduction on Earth's polar regions in

2006, it is now bigger.

Scientists started studying this layer in the late seventies. The first data estimated it around 5% from 1979 to 1990. The reduction is mainly due to a catalytic reaction (a chemical reaction through which the reaction speed changes due to the intervention of substances) of the halogenated compounds that reach the stratosphere, despite the higher air density. It also occurs because of the global redistribution of the ozone that tends to deplete or to enrich the layer.

Its function is to absorb almost all the harmful ultraviolet radiations, in particular the UVB (95%) and the UVC (100%), although it lets almost completely penetrate the UVA rays. Therefore, if the layer is reduced, the amount of radiation that reaches the Earth's surface increases. These radiations are not harmful in minimal quantities; for example, they are useful in vitamin D skin synthesis. At higher doses, however, these ultraviolet rays have deleterious effects on the life of microorganisms, animals, plants and even plastics.

- **Greenhouse effect**. The greenhouse effect is the process by which radiations from a planet's atmosphere warm the planet's surface to a temperature higher than it would be without this atmosphere. Radiatively active gases (i.e., greenhouse gases) in a planet's atmosphere radiate energy in all directions. Part of these radiations are directed towards the surface. The intensity of the downward radiations, which is the level of the greenhouse effect, depends on the atmosphere's temperature and on the amount of greenhouse gases that the atmosphere contains. The greenhouse effect, as a natural phenomenon, is essential for the presence and development of life on Earth. The rise in the greenhouse effect, on the other hand, may alter the normal thermal equilibrium of the planet. The human intervention on nature over the years, though, has led to devastating climatic and environmental upheavals, including the so-called global warming.

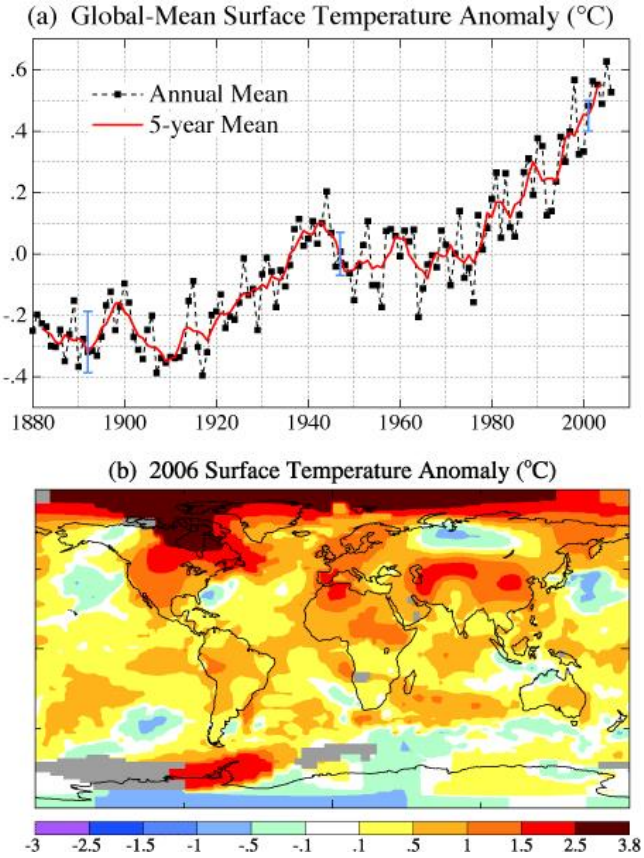

Figure 1.3: Effect of the global warming the world. (Source: "NASA", 2006)

The global temperature has risen by 0.8 degrees Celsius since 1880 according to NASA data, but about two thirds of the heating was consumed only from 1975 to the present: a growth rate of 0.15-0.20 degrees Celsius to decade.
At this rate, the Intergovernmental Panel on Climate Change (IPCC) warns, there could be a growth of 1.5 degrees Celsius between 2030 and 2052. The already critical threshold risks being crossed even further. Some data shown of an increase between 2.8 and 5.6 degrees Celsius over 85 years.
The consequences of this phenomenon are: the ice melting in the Arctic and Antarctic areas, with a subsequent rise in sea levels (figure (1.4)); expansion of the oceans, erosion of coastal regions and floods; the multiplication of extreme meteorological phenomena; deterioration of air quality and concentration of precipitation in limited periods of the year; famines and periods

of drought, with deleterious consequences on food and water resources.

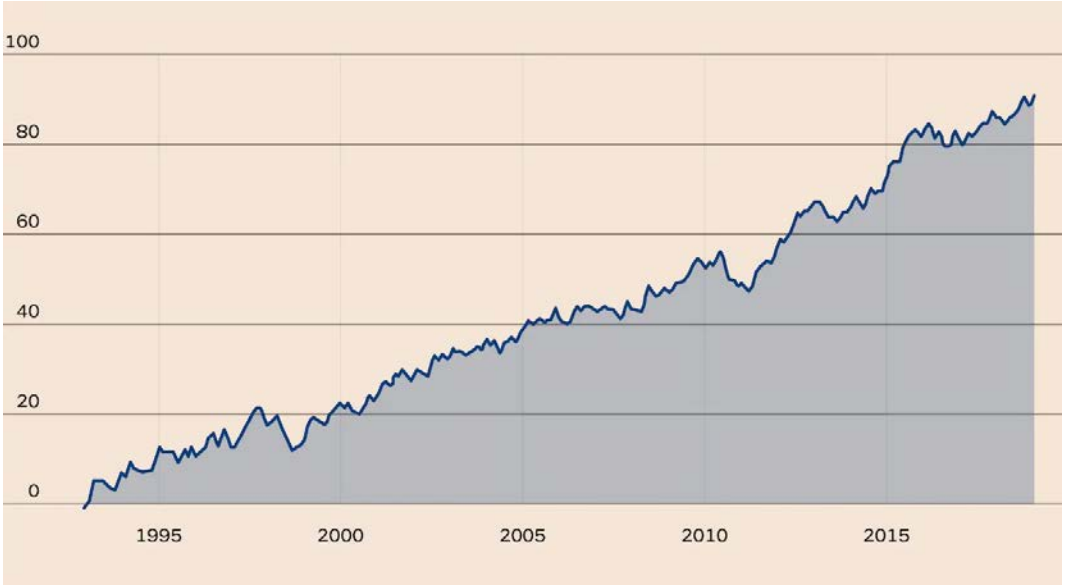

Figure 1.4: Sea level rise trend. (Source: "Il Sole 24 Ore", 2019)

- **Acid rain**: It is a rain or any other form of precipitation that is unusually acidic, meaning that it has elevated levels of hydrogen ions (low pH, usually less than 5, because rain is always a little bit acid as the pH swings between 5 and 7). It can have harmful effects on plants, aquatic animals and infrastructure. Acid rain is caused by emissions of sulphur dioxide and nitrogen oxide, which react with the water molecules in the atmosphere to produce acids.

1.3 Aircraft Pollution

Civil and commercial aviation plays an irreplaceable role in connecting people from one end of the planet to the other. However, all this has a significant cost from an environmental point of view. Air transport causes greenhouse gas emissions (CO_2, N_2O and CH_4) and polluting gases (NO_x, CO, NMVOC and SO_2), in

addition to the release of particulate material PM_{10} and $PM_{2.5}$, arsenic, chromium, copper, nickel, selenium and zinc. According to an estimate by the Greenpeace, civil aviation alone generates globally around 600 million tons of CO_2 per year. A group of experts recently raised the estimate to 4.9%, revising the previous estimate which stood at 3%. Furthermore, airplanes emissions cause greater damage to the climate as they are released at high altitudes. All this is compounded by the fact that there was an increase of 8% in the number of flights in the period between 2014 and 2016, with a subsequently increase in the emissions and pollution. According to some estimates, airspace traffic, which has been growing steadily since 2005, will increase by 42% between 2017 and 2040, with additional consequences for air pollution. For example: an airliner pollutes as much as 600 Euro 0 vehicles, so the main Italian airports produce every day the same amount of emissions of around 350 thousand Euro 0 vehicles. In particular, it is believed that by 2040 the CO_2 and NO_x emissions will register a minimum increase of 21% and 16% respectively. For this reason, the research is going towards "all electric" aircraft. This concept is known as "More Electric Aircraft" (MEA).

Chapter 2

More Electric Aircraft (MEA)

The "all-electric" aircraft is not a new concept: it has been considered by military aircraft designers since World War II. For example in the '50s, the Bristol Brabazon and the Vickers Valiant V-Bomber utilized a great number of electrical systems. Until recently, though, the lack of electrical power generation capability, together with the volume of the power conditioning equipment and the advanced control required, rendered the approach unfeasible - especially for commercial and civil transport applications (Rosero et al. 2007).

Over the past decades, a number of aeronautical agencies in the US has been promoting the analysis of the benefits of all- electric aircraft. In the early '80 NASA funded a number of studies addressing the Integrated Digital Electrical Airplane (IDEA). The IDEA researches embraced a range of technologies which could improve efficiency of a 250-300 seater replacement for an aircraft (Moir and Seabridge 2008). The IDEA concept covered the following areas: Flight Control Technology (stability augmentation), Wing Technology (use of efficient high aspect ratio wings), Engine Power Extraction (reduction of engine power extraction), Flight Control Actuation (use of electro-mechanical actuation), and Advanced Electrical Power Systems (development of new electrical power system).

Then, in the early 1990s, the research focused on elimination of centralized hydraulics aboard to replace them with electrical power. With this aim several programs were started: Totally Integrated More Electric Systems (TIMES) to use

previously developed systems into electrical aircraft and US Air Force MEA Program to provide more electrical capability.
In the first two years of 2000, the studies aimed to reduce the aeroplane weight, fuel consumption, power take up and the maintenance costs. In fact, the MESA (Magnetostrictive Equipment and Systems for more electric Aircraft) and the POA (Power Optimised Aircraft) projects were launched with that target.
In 2004, the MESEMA (Magnetoelastic Energy Systems for Even More Electric Aircraft) project developed and tested the innovative transducer systems to generate high-torque and electrical energy, and to reduce vibration and noise. This project evolved in two European research programs named "MADAViC" and "MESA" based on the six years scientific and technological objectives reached by the MESEMA (Boglietti et al. 2009).
In 2006 the MOET (More Open Electrical Technologies) project tried to set the new industrial standard for commercial aircraft designing, moving from the "fly-by-wire" to the "power-by wire" concept.
Today MEA has an important role in the researches managed by the CleanSky, a public-private partnership between the European Commission and the European aeronautics industry, that coordinates and funds research activities to deliver significantly quieter and more environmentally friendly aircrafts.
All these studies have contributed to create various electrical equipment that are used in the Airbus A380 and in the Boeing B787, which we will discuss in details in the following paragraphs.

2.1 Aircraft Today

Conventional aircraft architectures are a combination of systems that rely on mechanical, hydraulic, pneumatic, and electrical sources, and on fuel that is converted into power by the engines.

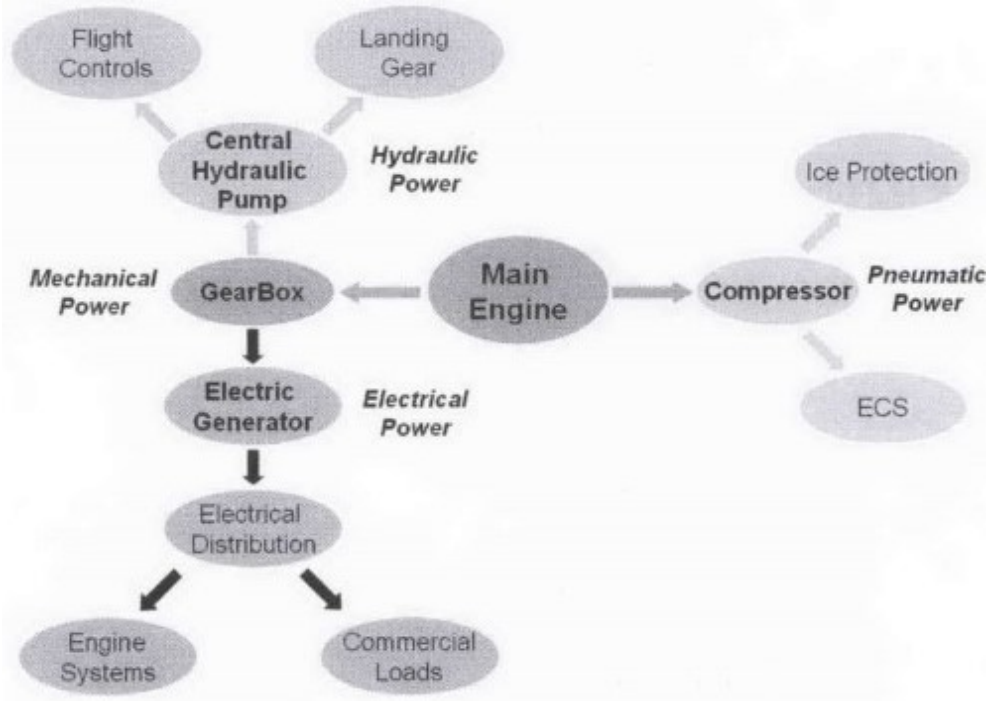

Figure 2.1: Block diagram of the main conventional aircraft architectures. (Source: Rosero et al. 2007)

Most of this power is used as propulsive power to move the aircraft. The remainder is converted into various forms:

- **Electrical System**. An aircraft electrical system supplies electrical power to the hydraulics, environmental-control, avionics, lighting and other subsystems. The electrical system consists of batteries, generators (located near the engine and alternating current AC is provided), transformer-rectifiers (TR, that converts alternating current to direct current), electrical controls, circuit breakers and cables.

- **Hydraulics**. A simplified hydraulic system is shown in figure (2.2). An hydraulic fluid, a light oil-like liquid, is pumped up to a certain pressure and stored in an "accumulator".

  When the valve is opened, the hydraulic fluid flows into the actuator where it presses against the piston, causing it to move and in turn moving the con-

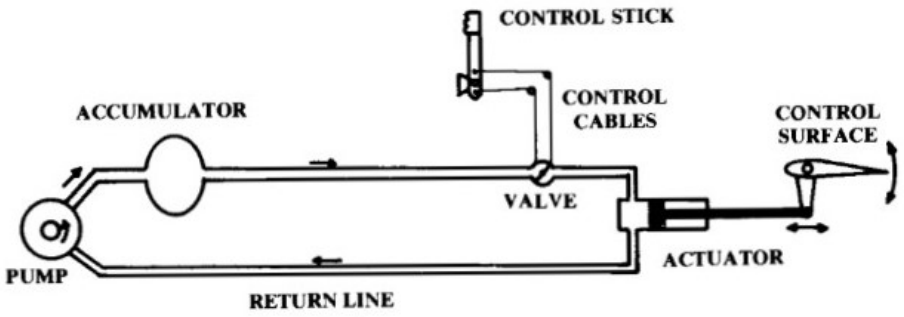

Figure 2.2: Simplified scheme of an hydraulic system. (Source: Raymer 2019)

trol surface. To move the control surface to the other direction an additional valve (not shown) admits hydraulic fluid to the back side of the piston. The hydraulic fluid returns to the pump through a return line. To obtain a rapid response, the valve must be very close to the actuator (Moir and Seabridge 2008), therefore it is attached to the actuator. There are two types of pilot's control inputs: the mechanic one (steel cables strung from the control pedals to the valves on the actuators) and the electronic one (in this case electromechanical valves are put, "fly-by-wire"). These types of system are used for flight control as well as the actuation of the landing gear, spoilers, weapon bays, speed brakes and flaps. The flight-control hydraulic systems have to include something to supply the proper control "feel" to the pilot, that is provided by a combination of springs, bobweights and air bellows.

- **Pneumatic System**. It provides compressed air for the anti-icing system, Environmental Control System ECS (cockpit pressurization and avionics cooling) and, in some cases, for the engine starting (usually, though, a battery starts the first engine). Typically, the air bleed that is used by this system comes from the engine compressor and it is cooled through a heat exchanger using outside air. Also, some military aircraft use a ground power cart that provides compressed air through a hose to start the engine.

- **Auxiliary/Emergency Power**. Large or high-speed aircraft are completely dependent upon the hydraulic system for flight control. In fact if the hy-

draulic pumps stopped producing pressure for any reason, this would cause an immediate loss of control of the aircraft. For this reason, it is required to have some form of emergency hydraulic power. Furthermore, the electrical power must be retained until the engines can be restarted. The three main emergency systems are:

1 **The Ram-Air Turbine (RAT)**. It is a windmill extended into the slipstream or a small inlet duct to admit air into a turbine.

2 **Monopropellant emergency power unit (EPU)**. It is used to drive a turbine a monopropellant fuels like hydrazine, even if they are all toxic and caustic. This kind of power system is, therefore, undesirable for operational considerations. However, the advantages are that it doesn't require any inlet ducts to provide immediate power regardless of the aircraft velocity, attitude and altitude. Monopropellant EPU's has to be located in a place where it avoids the caustic fuel puddles inside the aircraft.

3 **Jet-fuel EPU**. It is a small jet engine that drives a turbine to produce emergency power and to start the main engines ("jet-fuel starter"). This system requires an inlet duct, but it doesn't need a dangerous fuel like Monopropellant EPU. Many aircrafts use a jet-fuel Auxiliary Power Unit ("APU"), that is similar to an EPU but it is designed and installed to allow continuous operation (air conditioning, cabin lighting, and engine starting). Thanks to this, the aircraft is completely independent from any ground power carts. The APU is actually another jet engine. It is also used for emergency power and in some cases it is run continuously for further hydraulic and/or electrical power. This system requires its own inlet and exhaust ducts. As it needs fairly high maintenance firewalled structure and in order to avoid high levels of noise, the system should be directed upwards in an easily accessible place. Transport aircraft usually have the APU in the tail, away from the passengers compartment, because the exhaust duct is normally hot and noisy, as shown in figure (2.3). Fighters, on the other hand, usually

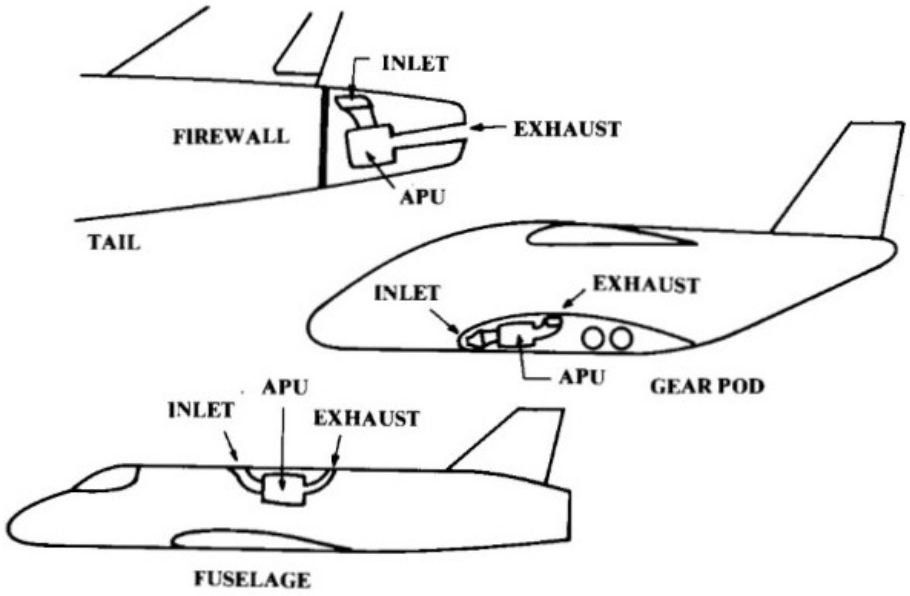

Figure 2.3: APU position in conventional aircraft structure.(Source: Raymer 2019)

have the APU in the fuselage, near the hydraulic pumps and generators, but this requires a firewall that encloses completely the APU.

- **Accessory drives**. Many high-performance aircraft have an AMAD (Airframe Mounted Accessory Drive), which is a special gearbox that connects all attached engine-driven accessories to the engine. In this way, if the engine has to be removed, there is no need to disconnect all the accessories as it is done for early aircraft, but only the engine.

- **Avionics**. It includes navigational aids, flight control computers, radar, and other aircraft sensors such as infrared detectors. They could be classified in:

  1 Communication and Navigation

  2 Mission Equipment

  3 Vehicle Management

While the first two are considered as "add-ons", because the aircraft would fly anyway without them, the third one is indispensable.

2.2 MEA aircraft

The three key methods for extracting energy from the engine in conventional aircraft have been:

- Electrical power by an accessory gearbox driven generator
- Hydraulic power by means of Engine Driven Pumps (EDPs)
- Pneumatic power got by bleeding air.

The latter is little efficient and, as the purpose is to fully realise the benefits of emerging engine technologies, it is necessary to design a more efficient mean to extract power.

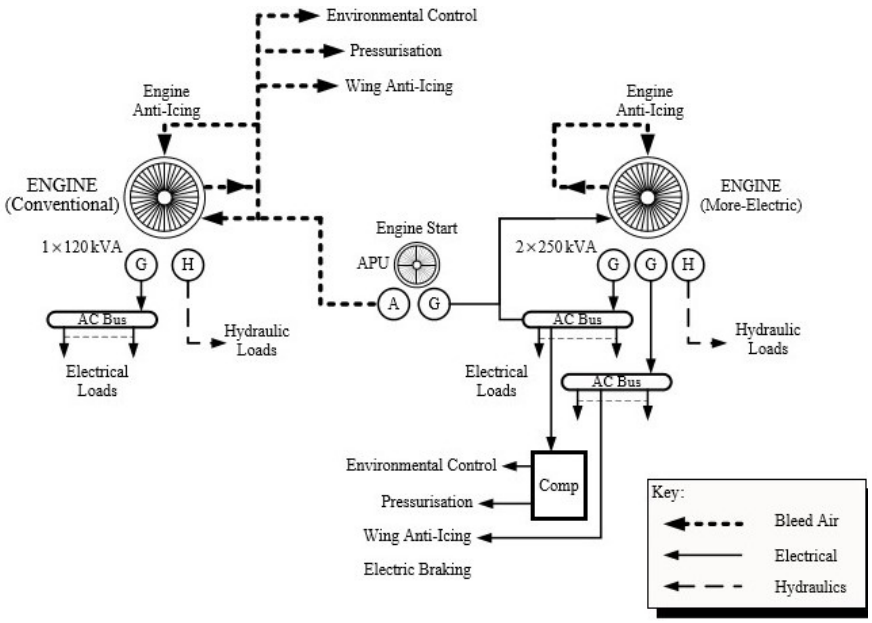

Figure 2.4: Different scheme between conventional and more electric aircraft. (Source: Moir and Seabridge 2008)

In the figure (2.4) the differences between conventional power extraction using bleed air on the left versus a more-electric version on the right are shown. These architectures represent the Boeing 767 (left) and the Boeing 787 (right). The principal differences are:

- **Reduced bleed air off-take**. The only bleed air off-take in the B787 is for engine anti-icing engine. Therefore it is more efficient than that extracted from the engine compressor.

- **Increased electrical power generation**. The B787 has a system that produces 500 kVA per channel instead of 120 kVA (B767). This difference of generated electrical power is used to provide energy to those systems no longer powered by bleed air.

- **Electric engine start**. The B787 has an electric start as bleed air is reduced and therefore it is no longer available for this purpose.

2.2.1 Electric System

The B787 electrical power system is illustrated in Figure (2.5). A key feature is the adoption of a three-phase 230 VAC electric power compared to the conventional three-phase 115 VAC solution universally adopted by the Industry. The increase in voltage by a factor of 2:1 decreases feeder losses in the electrical distribution system and it allows significant wiring weight reduction. The use of higher 230 VAC phase voltage, or 400 VAC line-to-line, requires considerable care during the design to avoid the possible effects of partial discharge, also known as 'corona'.
The more important characteristics of the B787 electrical power system are:

- Starter/generators. They generate 2x250 kVA per engine, resulting in 500 kVA per channel, with variable frequency, as recent industry trends are moving away from constant frequency 400 Hz power

- 2x225 kVA APU starter/generators. Each starter/generator after starting the APU acts as a generator during normal operation.

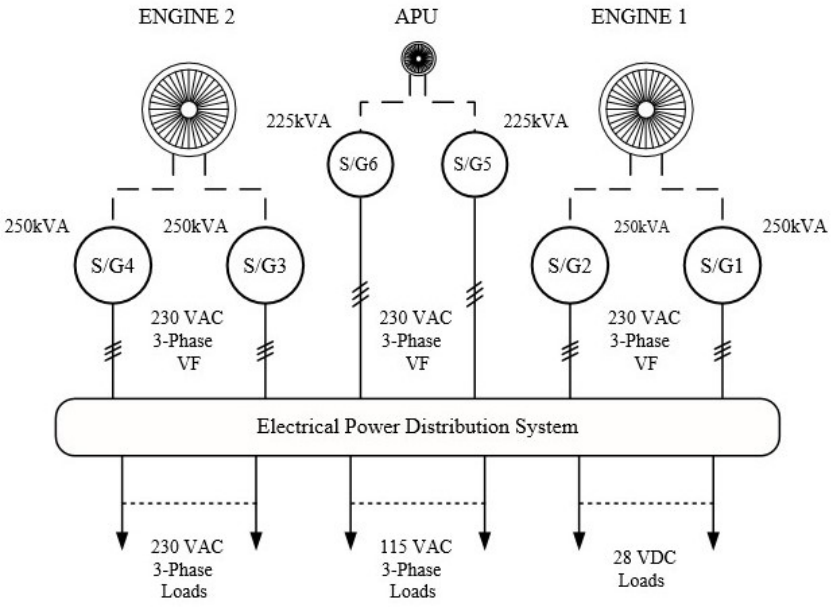

Figure 2.5: Electrical scheme for B787 aircraft. (Source: Moir and Seabridge 2008)

- Before being fed into the power distribution system, each principal generator feeds its own 230 VAC main bus. Then, according to the load, it is either converted into 115 VAC and 28 VDC power to feed the subsystems or it remains unchanged.

As it is shown in the figure (2.6), the bleed air is no longer used (only to perform an anti-icing function for engine), so the environmental control system, cabin pressurisation system, wing anti-icing system as well as other air-powered subsystems are not fed. Removing bleed air off-takes has dual advantages: decreasing the engine compressor waste; avoiding the use of large ducts throughout the airframe to transport the air they would require the removal of the overheads. The main more-electric loads in the B787 system are:

- **Environmental Control System (ECS) and pressurisation**. The removal of bleed air means that the electrical system has to pressurise the air thanks to four compressors which requires about 500 kVA.
- **Wing anti-icing**. Electrical heating mats embedded in the wing leading edge (consumption about 100 kVA) provide the energy to feed that system.

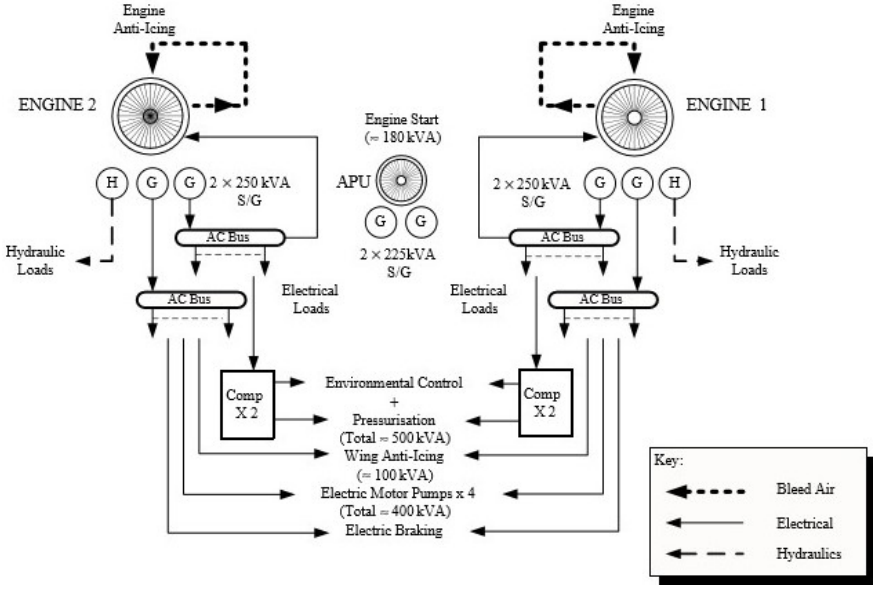

Figure 2.6: Electrical loads in B787. (Source: Moir and Seabridge 2008)

- **Electric motor pumps**. Some of the aircraft hydraulic Engine Driven Pumps (EDPs) are replaced by electrically driven pumps (four new electrical motor pumps that requires about 100 kVA each giving a total load requirement of 400 KVA)

Furthermore, the engines use the in-built starter/generators for this purpose and require about 180 kVA to start the engine.

2.2.2 Hydraulic System

The effects of using the new aircraft architectures are shown in the figure (2.7) that illustrates the hydraulic system differences for the Boeing 767 (conventional Boeing wide body) versus the more electric Boeing 787.

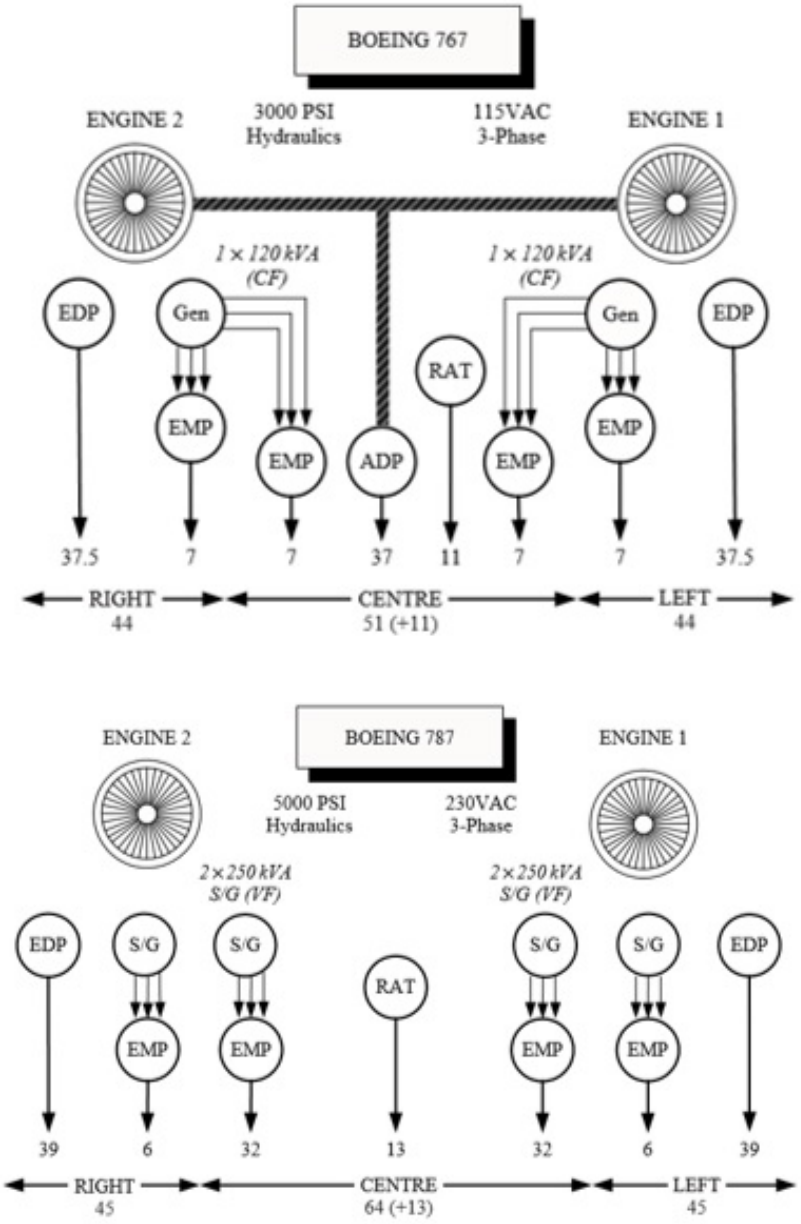

Figure 2.7: Differences between the B767 and the B787 hydraulic system. (Source: Moir and Seabridge 2008)

Both architectures use the Boeing Left (L), Centre (C), Right (R) hydraulic channel philosophy. The main differences are:

- Engine bleed air is eliminated with the removal of the Air Driven Pump (ADP)
- The use of 5000 psi ($3,4474 \cdot 10^7$ Pa) rather than 3000 psi ($2,0684 \cdot 10^7$ Pa) hydraulics system
- The adoption of 230 VAC, three-phase, VF primary power rather than 115 VAC, three-phase 400 Hz CF
- The use of starter/generators versus generators to facilitate the electric engine start
- Use of larger Electric Motor Pumps (EMPs), around four times that of the previous units.

Generally, levels of electrical power are increased, in fact the primary channel moved from 120 kVA to 500 kVA.
This type of system is more conservative than the '2H+2E' system adopted on the Airbus A380. In fact some hydraulic channels have effectively been replaced by a channel using distributed electrically powered actuation.

2.2.3 Environmental System

The figure (2.8) shows the different ECS and pressurisation system with electrically driven compressors with no bleed air mean.
Like most aircraft of this size, the B787 is fitted with two air-conditioning packs. The main difference is that they are electrically powered by four electrical driven motor compressors (two for each pack) controlled by two motors/controllers (one for each pack requiring 125 kVA). The outputs from these compressors enter a common manifold before being fed through primary and secondary heat exchangers (cooled by external ram air as would be the case in a conventionally driven Air

Cycle Machine "ACM"). After this process, the air is mixed with recirculation air to maintain the desired temperature.

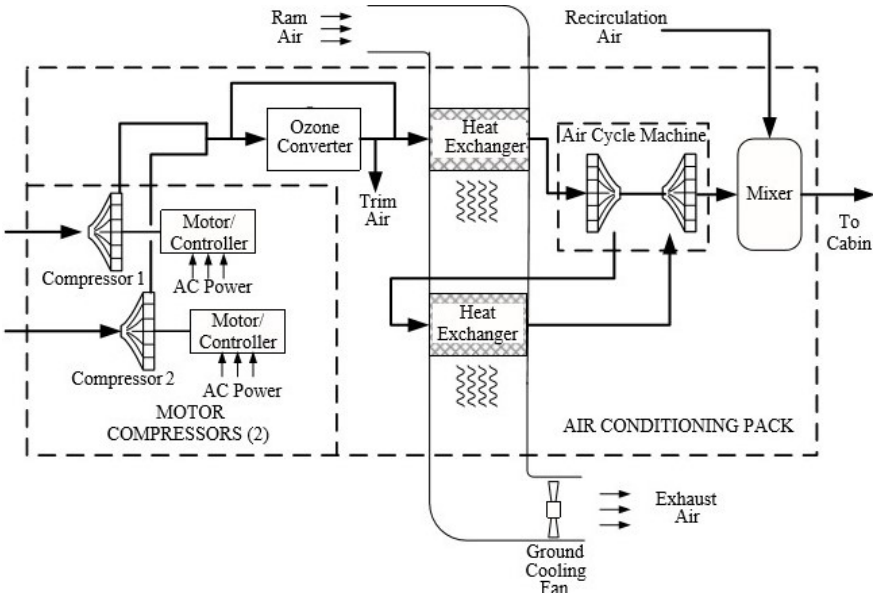

Figure 2.8: ECS and pressurisation system for the B787. (Source: Moir and Seabridge 2008)

Although the power required for this system is high, the advantages are that: the bleed air extracted from the engine's central core is removed, and the temperature and pressure of the air is considerably lower.
The figure (2.9) shows the differences between a conventional and an electrical ECS. Engine bleed air enters in ECS system at about 400° F and at about 30 psi, while in the other configuration at about 200° F and a lower pressure of 15 psi. After being cooled by the air cycle machine the typical output will be around 60° F and 11.8 psi. The energy expended differs greatly between the two methods; this difference represents the energy loss and waste. These more-electric systems require new technologies:

- The electrical power distribution cabinets that are located in the forward and aft EE bays weigh about 1000 lbs each

- Large loads necessitate dedicated motor controllers
- In many cases +/-270 VDC power is used within these cabinets
- The cabinets are liquid cooled due to the significant heat dissipation.

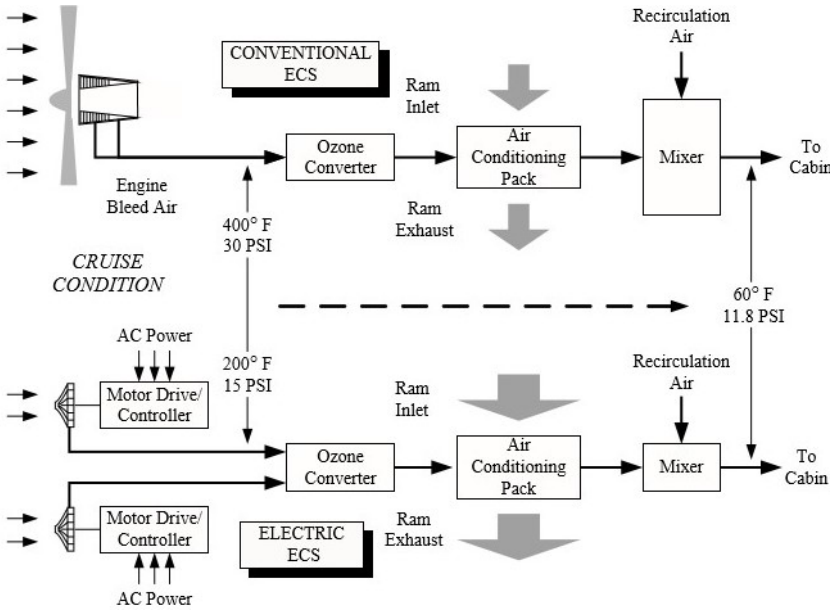

Figure 2.9: Differences between the B767 and B787 ECS system. (Source: Moir and Seabridge 2008)

2.3 Type of candidate Machine for MEA

The electrical motor is a main component in any electrical drive system. In the aerospace applications it has specific stringent requirements for reliability and power density. In view of the machine design, the following requirement should also be fulfilled:

1 Mechanical, electrical, thermal and magnetic isolation between lanes

2 High torque/weight ratio and high torque/ampere ratio

3 High value of the phase inductance (for PM motors)

4 High efficiency throughout the full speed range.

Electrical machines with brushes or commutators are not taking into consideration because they have: low torque density, high maintenance requirements and lack of reliability.
Accordingly, the candidate machines are induction, reluctance, and PM motors, as shown in figure (2.10).

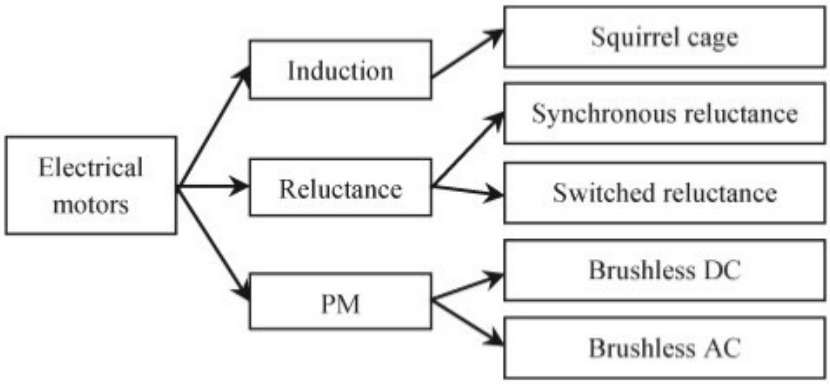

Figure 2.10: Block diagram of candidate electrical motors for more electric aircraft. (Source: Cao et al. 2012)

2.3.1 Induction motor

Squirrel-cage induction motors are simply, rugged, cheap and reliable, for this reason they are used extensively in aerospace industry. However, mutual coupling among all phases and the rotor makes it virtually impossible to fulfil the first requirement listed above.
Even if, in literature, several multiphase induction motor drives have been developed in a modular configuration, which decreases the interphase electrical and magnetic couplings and improves their fault tolerance, the penalty is the necessity for more complicated control techniques. In fact, it may be difficult to implement and synchronize them, due to the safety requirement to separate control electronics

and processing for each phase. These motors are able to continue their operations following an open-circuit failure, but they cannot operate after short-circuit failure.

2.3.2 Reluctance motor

The reluctance motor presents a robust rotor structure which uses neither windings nor PMs and which is able to withstand mechanical or thermal stresses. Therefore, it is a machine for low-cost applications.
In the synchronous reluctance motor rotor saliency is created either by salient poles or by adding internal flux barriers that guide the magnetic flux along the direct axis. Once synchronous speed is reached, the rotor does not present any induced electromotive force (emf). The motor is more efficient than induction motors due to the removal of the rotor joule loss. Stator windings are similar to that of induction motors, because they are sinusoidally distributed around the air-gap. They develop strong mutual coupling between phases, it does not fulfil the first criteria and it is poor fault tolerance.
The switched reluctance (SR) motor, on the other hand, is more and more used in direct drive applications and it is a good choice in aerospace industry for its natural fault tolerance capability. Its saliency is on both the stator and rotor, and it has inherently independent phase windings. Separate simple converter topology (two switches per phase) is commonly adopted as unipolar excitation currents are used. This configuration gives further independence between phases and more stability with the presence of a short circuit, that can still operate with a reduced mean torque capability. In addition to these shoot-through faults caused by the converter switches are eliminated, thanks to the series connection of the converter phase-leg switches with the SR motor phase winding.
A four-phase 8/6 SR topology is a good compromise between fault tolerance and complexity for aerospace application. Anyway, if it happens that one of the four phases faults, it will not be possible to develop full torque at all rotor positions. This could cause problems for many actuation applications. Because both magnetizing current and torque-producing current must be supplied by the stator windings, SR motors are approximately 50% larger than an equivalent PM motor. There is some

debate as to whether SR motors can be made smaller than induction motors of similar capability. SR motors certainly have much smaller end windings, less coupling between phases, and lower rotor loss, which has generally resulted in them being regarded as preferential to induction machines for fault-tolerant aerospace applications (Cao et al. 2012).

2.3.3 Permanent magnet motor

PMACs (acronym that covers all brushless ac permanent magnet motor) have: high torque/inertia, high power density and efficiency, torque/volume ratios, and improved reliability.
In this type of machine the rotor can have different arrangements, but surface-mounted PM motors is used for its small rotor diameter with low inertia, whereas interior permanent magnet motors generate higher per unit inductances and therefore field weakening capability. In addition, deep PMs and a single-layer concentrated winding topology are designed to increase fault tolerant capability, as the mutual inductance decreases.
They are less intrinsically fault tolerant than REL and induction motors, but they develop higher torque density. PMAC's problem is that currents can flow in a failed lane (also a disconnected one), because there is a magnet-induced back emf. It can be resolved by a careful parameter selection. For example the inductance, because the resulting current can be limited to no more than rated current, even if at low speed a drag torque is generated.

Chapter 3

MEA motor's analysis

Summing up all the data explained in the previous chapter, the results are:

Performance	**IM-cage**	**SR**	**PMAC**
Fault-tolerant	low	high	high
Power density	moderate	moderate	high
Robustness	✓	✓	X
Efficiency	moderate	high	high
Cost	low	low	high
Wide range speed	X	✓	✓
Open-loop control	✓	X	X
Close-loop simplicity	✓	✓	✓
Torque ripple	X	high	low

Table 3.1: Characteristics of the candidate electrical motor for more electric aircraft. (Data source: Cao et al. 2012)

So, we chose to study the SR and the PMAC motors for their best characteristics.

3.1 Motors

3.1.1 PMAC

Surface-mounted permanent-magnet machine can be considered as a synchronous machine in which the rotor excitation winding is constituted by a permanent magnet. This configuration permits to reduce the encumbrance of the rotor and to eliminate almost completely Joule losses of the excitation. The system, composed by a permanent magnet synchronous motor, its power supply and its control system, is usually defined "brushless motor". The magnet on the rotor can be external or internal.
In this case we chose an exterior permanent magnet rotor and the data motor are taken from the paper by Andrea Cavagnino (Senior Member, IEEE), Zijian Li, Alberto Tenconi (Senior Member, IEEE) and Silvio Vaschetto (Member, IEEE).

Physical quantity	**Unity of measurement**	**Value**	**Symbol**
Number of phases		6	m
Rated torque	Nm	1200	τ_m
Rated speed	rpm	2400	Ω
Rated voltage	V	134	V_n
Rated current	A_{rms}	443	I_{rms}
Frequency	Hz	600	f

Table 3.2: Permanent magnet motor data. (Data source: Cavagnino et al. 2013)

Geometrical data

Physical quantity	Unity of measurement	Value	Symbol
Shaft diameter	mm	100	D_{sft}
Internal stator diameter	mm	700	D_{si}
External stator diameter	mm	900	D_{se}
Internal rotor diameter	mm	904	D_{ri}
External rotor diameter	mm	980.4	D_{re}
Number of slots		36	Q
Active axial length	mm	70	L_{stk}
Air-gap height	mm	2	g
Slot height	mm	61.9	h_s
Slot area	mm^2	2067.46	S_{slot}
Slot width	mm	33.4	w_s
Slot opening width	mm	3	w_{so}
Slot opening height	mm	9.5	h_{so}
Magnet thickness	mm	12	t_m
Magnet Length	mm	83.4	w_m

Table 3.3: Permanent magnet motor geometrical data. (Data source: Cavagnino et al. 2013)

In addition to this, the rotor and stator sheets are made of a cobalt-iron alloy, whose the saturation is also considered in the B-H curve reported below:

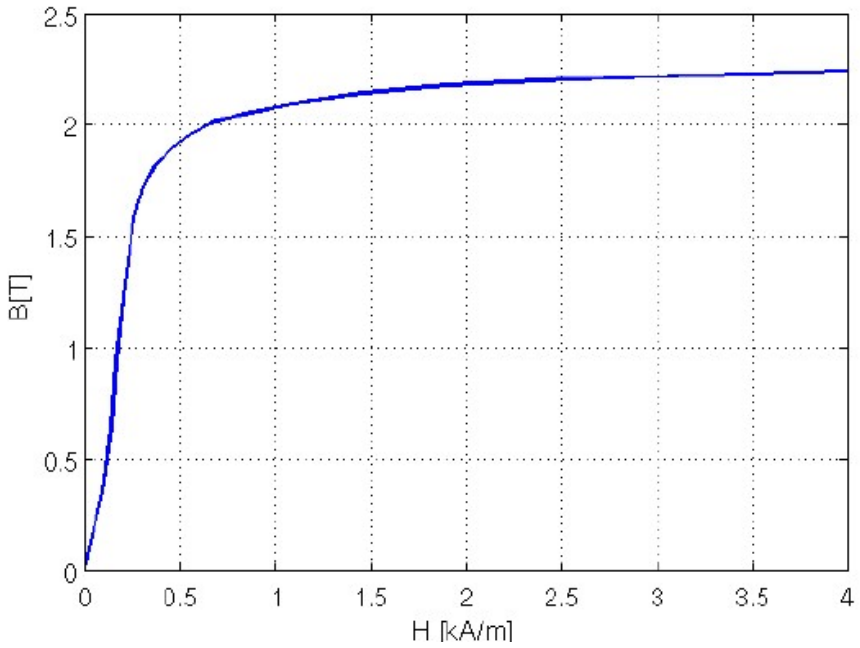

Figure 3.1: Cobalt-iron B-H characteristic. (Source: Gudmundsson 2019)

While it is used Sm_2Co_{17} magnet for which it is reported the CIBAS' datasheet:

		Sm_1Co_5	Sm_2Co_{17}
Br TEMPERATURE COEFFICIENT*	% / °C	- 0,045	- 0,035
HcJ TEMPERATURE COEFFICIENT*	% / °C	- 0,19	- 0,24

Figure 3.2: Sm2Co17 datasheet first part. (Source: "CIBAS", 2019)

Sm_2Co_{17}

GRADES	Br		HoB		HoJ		BH max		Max. Working Temp.**
	G	T	Oe	kA/m	Oe	kA/m	MGOe	kJ/m³	°C
RES 207 / 143	10.300 - 10.800	1,03 - 1,08	9.500 - 10.200	756 - 812	≥ 18.000	≥ 1.433	26 - 28	207 - 223	≤300
RES 223 / 143	10.800 - 11.000	1,08 - 1,10	9.900 - 10.500	788 - 835	≥ 18.000	≥ 1.433	28 - 30	223 - 239	≤300
RES 231 / 143	11.000 - 11.500	1,10 - 1,15	10.200 - 10.800	812 - 860	≥ 18.000	≥ 1.433	29 - 32	231 - 255	≤300
RES 207 / 199	10.300 - 10.800	1,03 - 1,08	9.500 - 10.200	756 - 812	≥ 25.000	≥ 1.990	26 - 28	207 - 223	≤350
RES 223 / 199	10.800 - 11.000	1,08 - 1,10	9.900 - 10.500	788 - 835	≥ 25.000	≥ 1.990	28 - 30	223 - 239	≤350
RES 231 / 199	11.000 - 11.500	1,10 - 1,15	10.200 - 10.800	812 - 860	≥ 25.000	≥ 1.990	29 - 32	231 - 255	≤350

Figure 3.3: Sm2Co17 datasheet second part. (Source: "CIBAS", 2019)

As it is not specified in the chosen paper, for this thesis we will considered RES 207/143. Furthermore, we will take into account the linear B-H characteristic of this material with a constant angle for each operating temperature. In this way, the slope is constant and therefore it is considered a sheaf of straight lines.

Winding

The winding presents a duplex three-phase configuration, because it increases the fault tolerant capability. In this way, the motor can still work with less current value (also torque value) during a fault, while in state operation each winding can provide half current.
The project of the winding starts from the determination of the star of slot that permits to find the slot matrix. This is used in the FEMM analysis, because it permits to locate the winding arrangement.
In this case we ha have a winding 36 slots/30 poles according to the paper that the number of slot per pole per phase (q) is $\frac{2}{5}$, so the eddy-current losses in the rotating parts are limited.
The highest common denominator is:

$$t = H.C.F.\{Q, p\} = H.C.F.\{36, 15\} = 3 \tag{3.1}$$

The mechanical angles is:

$$\alpha_s = \frac{360}{Q} = \frac{360}{36} = 10° \tag{3.2}$$

while the electrical one is:

$$\alpha_s^e = p \cdot \alpha_s = 15 \cdot 10 = 150° \tag{3.3}$$

The periodicity of the star of slots is:

$$\frac{Q}{t} = \frac{36}{3} = 12 \tag{3.4}$$

Knowing that the phases are 60° apart:

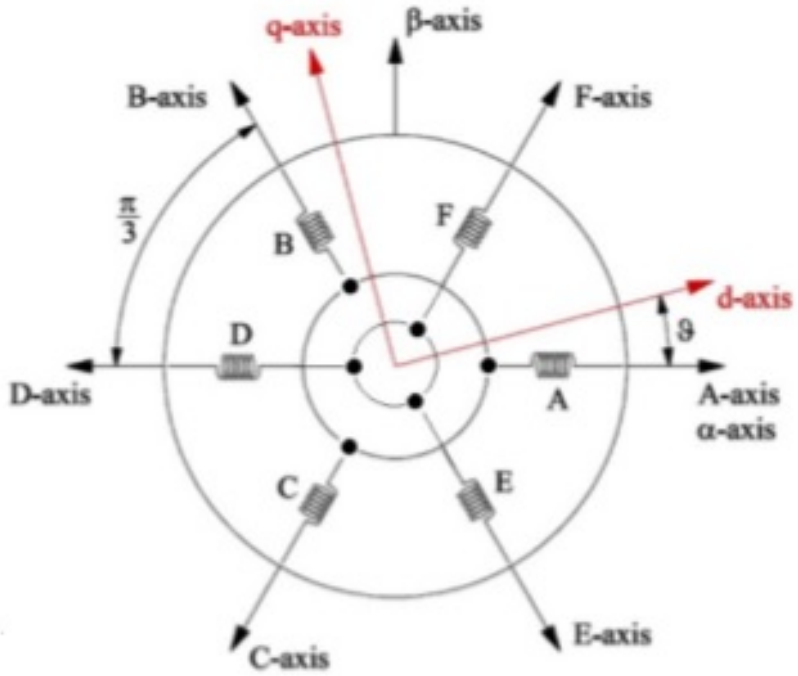

Figure 3.4: Positioning of the various phases. (Source: Cavagnino et al. 2013)

The star of slots for the first winding is:

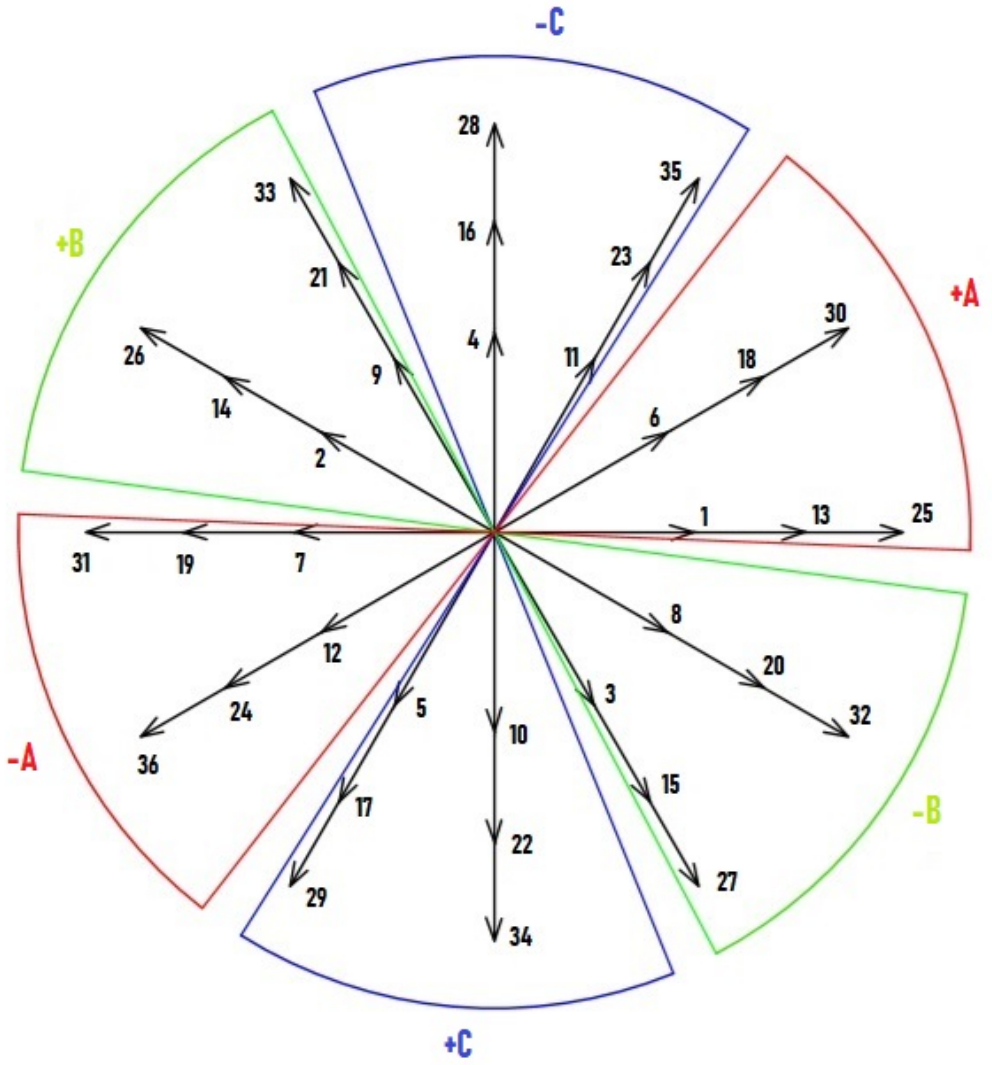

Figure 3.5: Star of slots of the first winding.

while the second one becomes:

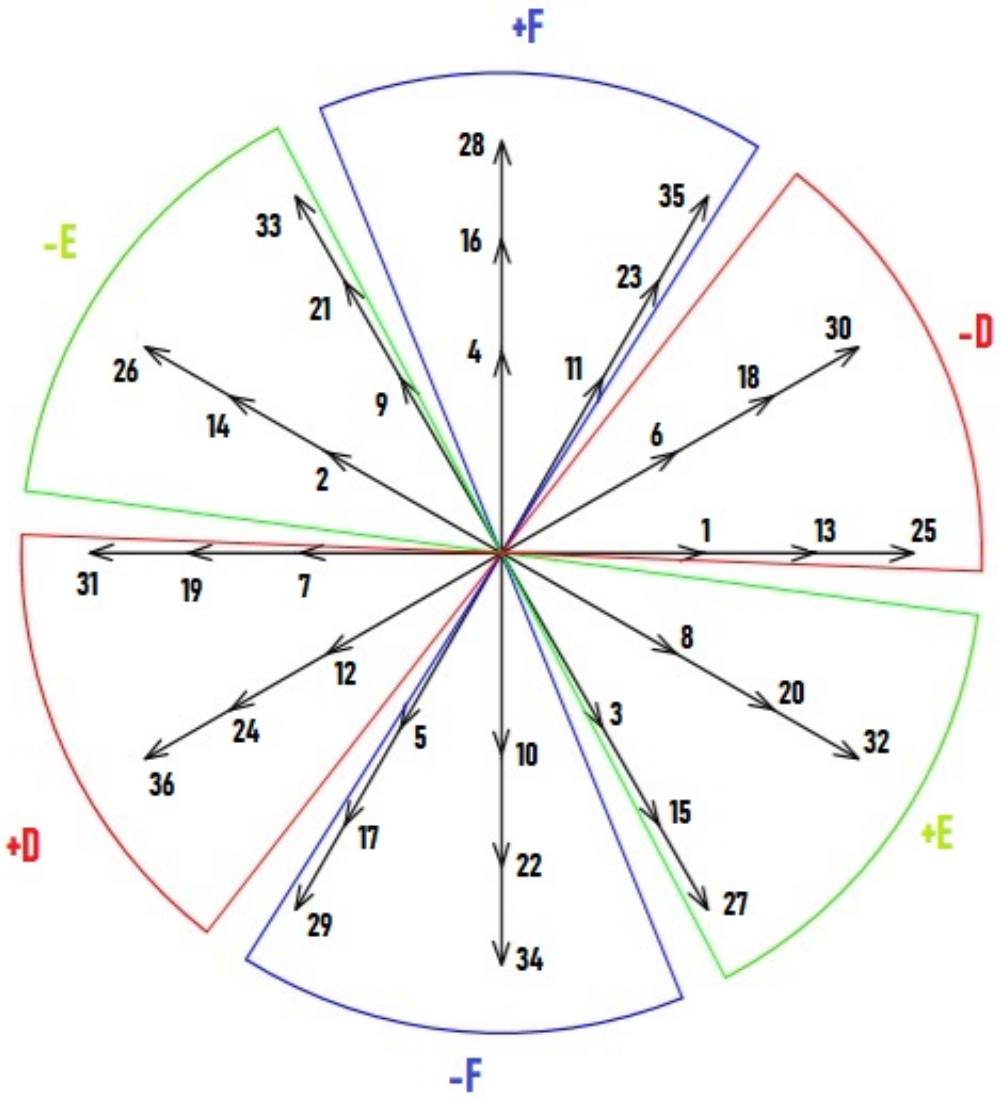

Figure 3.6: Star of slots of the second winding.

Going on with the studies of the winding, the winding factor has to be calculated. To do this, we have to compute the distribution factor (K_d) and the pitch factor (K_p).

Knowing that $q = \frac{2}{5}$ and $\alpha_s^e = 150°$, the distribution factor is:

$$K_d = \frac{sin(q \cdot \frac{\alpha_s^e}{2})}{q \cdot sin\frac{\alpha_s^e}{2}} = \frac{sin(\frac{2}{5} \cdot \frac{150}{2})}{\frac{2}{5} \cdot sin(\frac{150}{2})} = 1.294 \tag{3.5}$$

As it is not specified in the paper, the pitch angle β_p is equal to 0°.
Therefore, the pitch factor is:

$$K_p = cos(\frac{\beta_p}{2}) = cos(\frac{0}{2}) = 1 \tag{3.6}$$

So, we are able to compute the winding factor as follows:

$$K_w = K_d \cdot K_p = 1.294 \cdot 1 = 1.294 \tag{3.7}$$

This value is incorrect, as K_w is a factor that is less than 1.
I tried to contact the author of the paper, but the data are protected.
For this reason, we have to find the correct value of β_p to decrease the value of the winding factor as less than the unity.
So, we want to find the minimum value of β_p to decrease K_w to 1.

$$K_w = K_d \cdot K_p;$$
$$K_p = \frac{K_w}{K_d};$$
$$K_p = cos(\frac{\beta_p}{2});$$
$$\frac{\beta_p}{2} = arccosh(K_p);$$

Therefore:

$$\beta_p = arccosh(K_p) \cdot 2 = 39.39 \cdot 2 = 78.8° \tag{3.8}$$

So, β_p has to be larger than 78.8° in order to decrease K_w.
For this thesis, we choose β_p=90°, in this way we obtain:

$$K_p = cos(\frac{\beta_p}{2}) = cos(\frac{90}{2}) = 0.707 \tag{3.9}$$

and therefore:

$$K_w = K_d \cdot K_p = 1.294 \cdot 0.707 = 0.915 \tag{3.10}$$

No-load operation

In this paragraph we analyse the motor in no load operation considering only the contribution of the permanent magnet to the air-gap flux and that the stator current equal to zero .

First of all, we have to define the number of conductors that the motor needs.

In the paper it is written that there are eight conductors in each half stator slot (n_c), 64 conductors in series per phase (N_s) in duplex three-phase configuration (128 in three-phase configuration), furthermore the total Litz conductor area is equal to 7.8 mm^2. Therefore:

$$n_{cs} = \frac{m \cdot N_s}{Q} = \frac{3 \cdot 64}{36} = \frac{16}{3} \tag{3.11}$$

To test if the values are correct we calculate the fill factor. This represents how much the slot is filled and it must have a value between 0.4 and 0.5.

$$K_{fill} = \frac{S_c \cdot n_c}{S_{slot}} = \frac{7.8 \cdot 8 \cdot 2}{2067.46} = 0.06. \tag{3.12}$$

The result is too small according to the factor range.

So, we chose to adjust its value by changing as few data as possible to be in line with the original research.

So, we give n_c the value of 60 and n_{pp} (value of parallel path) 15, that is the number of pair poles. In this way, we obtain:

$$n_{cs} = \frac{n_c}{n_{pp}} = \frac{60}{15} = 4 \tag{3.13}$$

$$N_s = \frac{Q \cdot n_{cs}}{m} = \frac{36 \cdot 4}{3} = 48 \tag{3.14}$$

and therefore:

$$k_{fill} = \frac{S_c \cdot n_c}{S_{slot}} = \frac{7.8 \cdot 60 \cdot 2}{2067.46} = 0.453 \tag{3.15}$$

After this, the value of the air-gap induction produced by the permanent magnets is calculated in order to determine the flux of the machine.

The air-gap induction is obtained by the formula:

$$\hat{B}_g = \frac{B_{rem} \cdot k_\sigma}{1 + \dfrac{g \cdot k_{cart} \cdot \mu_r \cdot k_\sigma}{t_m}} \tag{3.16}$$

where k_{sigma} and k_{cart} are two coefficient that take into account the form of the air-gap flux and the effect of the slots. The factor k_{sigma} is given by:

$$k_{sigma} = \frac{\tau_p}{\tau_p + 2 \cdot g} \tag{3.17}$$

where τ_p is:

$$\tau_p = \frac{\pi \cdot D_{re}}{2p} = \frac{\pi \cdot 0.9804}{2 \cdot 15} = 0.103m \tag{3.18}$$

So, we can calculate k_{sigma} with the formula (3.17):

$$k_{sigma} = \frac{0.103}{0.103 + 2 \cdot 2 \cdot 10^{-3}} = 0.963 \tag{3.19}$$

The Carter factor, instead, is given by the formula:

$$k_{cart} = \frac{p_s}{p_s + g - \frac{3}{4} \cdot w_{so}} \tag{3.20}$$

where:

$$p_s = \frac{\pi \cdot D_{re}}{Q} = \frac{\pi \cdot 0.9804}{36} = 0.086m = 86mm \tag{3.21}$$

So, we can calculate k_{cart} with the formula (3.20):

$$k_{cart} = \frac{86}{86 + 2 - \frac{3}{4} \cdot 3} = 1.0029 \tag{3.22}$$

Thanks to the CIBAS' datasheet, we know that B_{rem} is equal to 1.03T and μ_r is equal to 1.045. Therefore, we can calculate $\hat{B_g}$ with (3.16):

$$\hat{B_g} = \frac{1.03 \cdot 0.250}{1 + \frac{2 \cdot 1.0029 \cdot 1.045 \cdot 0.250}{12}} = 0.854T \tag{3.23}$$

So, the flux of the machine (linkage with one turn) is equal to:

$$\hat{\Phi} = \frac{\hat{B_g} \cdot Dre \cdot L_{stk}}{p} = \frac{0.854 \cdot 0.9804 \cdot 70}{15} = 3.91 \cdot 10^{-3} Wb \tag{3.24}$$

At the end, knowing that K_w is equal to 0.915, N_s equal to 48, the flux linked to a phase is:

$$\hat{\Lambda} = \frac{K_w \cdot N_s \hat{\Phi}}{2} = \frac{0.915 \cdot 48 \cdot 3.91 \cdot 10^{-3}}{2} = 0.11Vs \tag{3.25}$$

Load operation

In this paragraph, we analyse the load operation of the motor, when the stator windings are crossed by the current.
As we know the data motor, we can calculate the missing parameters for this study. First of all, we can calculate the angular speed by:

$$\omega_{m_0} = \frac{2 \cdot \pi \cdot f}{p} = \frac{2 \cdot \pi \cdot 600}{15} = 251.33 \frac{rad}{s} \tag{3.26}$$

Then, thanks to the rated torque and the mechanical speed, we can obtain the rated active power:

$$P_n = \tau_N \cdot \omega_{m_0} = 1200 \cdot 251.33 = 301.6kW \tag{3.27}$$

We can compute also the $cos(\phi)$ by:

$$P_n = \sqrt{3} \cdot V \cdot Irms \cdot cos(\phi)$$

Therefore, we have:

$$cos(\phi) = \frac{P_n}{\sqrt{3} \cdot V \cdot Irms} = \frac{301.6 \cdot 10^3}{\sqrt{3} \cdot 134 \cdot 443} = 3 \tag{3.28}$$

This result is not possible as the cosine function has values between 0 and 1.
For this reason, as it is not specified, we double both voltage and current, because there are two phases in each slot, therefore:

$$cos(\phi) = \frac{P_n}{\sqrt{3} \cdot V \cdot Irms} = \frac{301.6 \cdot 10^3}{\sqrt{3} \cdot 134 \cdot 2 \cdot 443 \cdot 2} = 0.73 \tag{3.29}$$

FEMM analysis

The FEMM finite element program allows to simulate the motor under examination to check the results recorded in the previous paragraphs.
In particular, the program discretizes the geometry of the motor and it calculates the magnetic potential vector A at each point of the domain. It is the basic parameter for determining all the magnitudes of our interest. Furthermore, greater attention must be paid in the air-gap as it requires a more complex mesh. The

geometry of the motor with its mesh is shown in this figure (3.7).

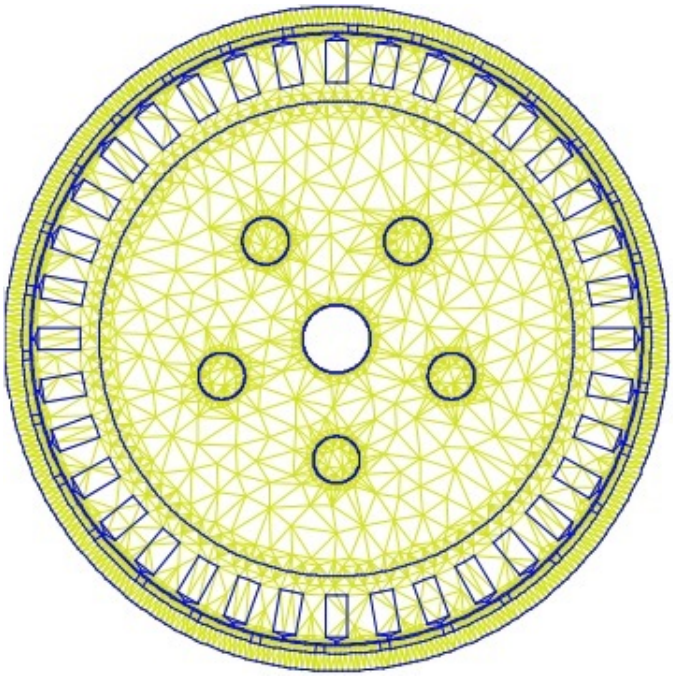

Figure 3.7: Geometry of the motor.

With this program we analyse again the no-load and load operation.
Beginning with no-load operation, we know that the motor is idle and for each rotor position we calculated the quantities we are interested in.
The first quantities of interest are the flux linkage to the six phases calculated with the following expressions:

$$\hat{\Lambda}_A = n_{cs} \cdot L_{stk} \cdot \sum k_a(i) \cdot \frac{1}{S_{slot}} \cdot \int A_z \cdot ds \tag{3.30}$$

$$\hat{\Lambda}_B = n_{cs} \cdot L_{stk} \cdot \sum k_b(i) \cdot \frac{1}{S_{slot}} \cdot \int A_z \cdot ds \tag{3.31}$$

$$\hat{\Lambda}_C = n_{cs} \cdot L_{stk} \cdot \sum k_c(i) \cdot \frac{1}{S_{slot}} \cdot \int A_z \cdot ds \tag{3.32}$$

$$\hat{\Lambda}_D = n_{cs} \cdot L_{stk} \cdot \sum k_d(i) \cdot \frac{1}{S_{slot}} \cdot \int A_z \cdot ds \tag{3.33}$$

$$\hat{\Lambda}_E = n_{cs} \cdot L_{stk} \cdot \sum k_e(i) \cdot \frac{1}{S_{slot}} \cdot \int A_z \cdot ds \tag{3.34}$$

$$\hat{\Lambda}_F = n_{cs} \cdot L_{stk} \cdot \sum k_f(i) \cdot \frac{1}{S_{slot}} \cdot \int A_z \cdot ds \tag{3.35}$$

where A_z is the magnetic potential vector that presents only the component along the z-axis (being the solenoid induction), and having components along x- and y-axis.

In the figures (3.8) and (3.9) it is shown the solution of field developed by FEMM with its flux lines as well as the density plot of the induction.

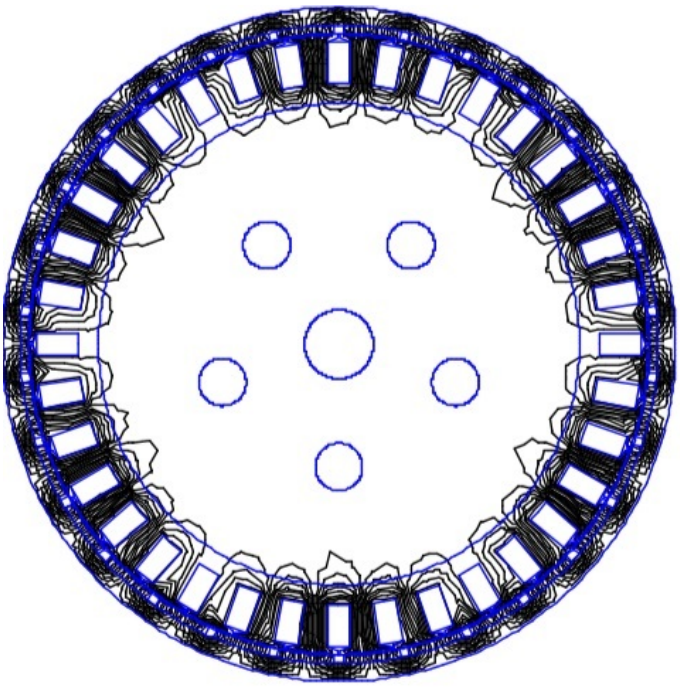

Figure 3.8: Flux lines in no-load operation.

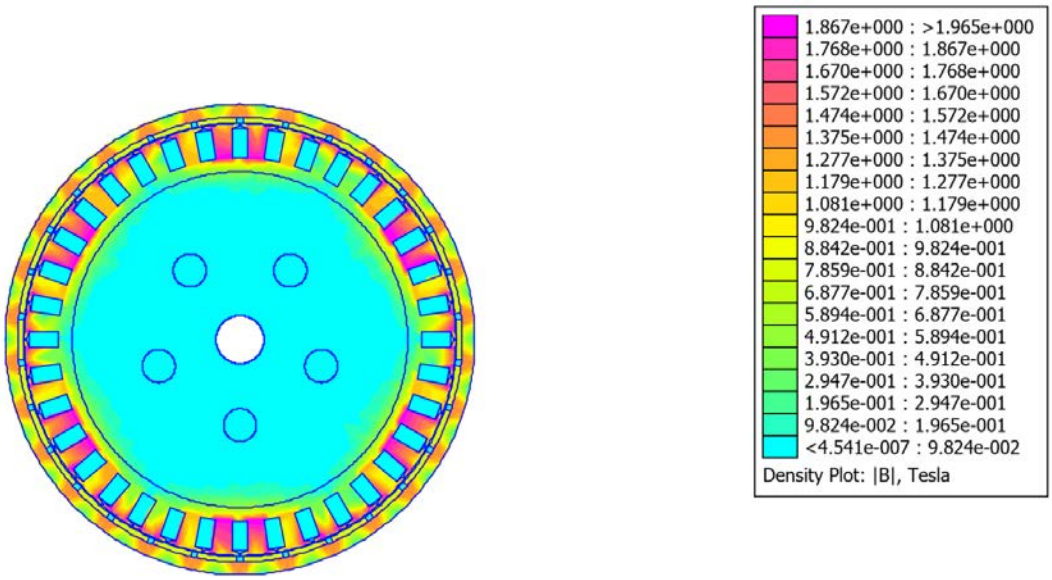

Figure 3.9: Induction density plot for no-load operation.

In the next pictures the trends of the flux linkage with the six phases are shown.

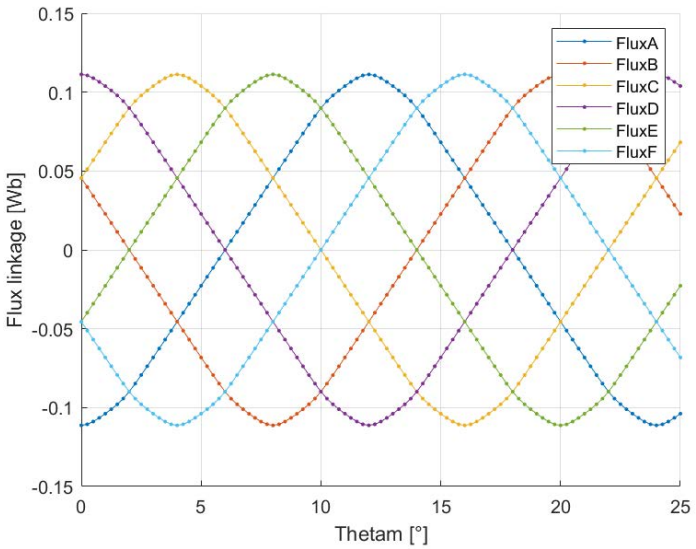

Figure 3.10: Trend of the flux linkage in no-load operation.

It can be noted that the maximum value of the flux is equal to the one we calcu-

lated before and the analysis is done when the maximum value of the flux linkage for A- and D-phase is reached.

After this, we calculate the trend of the no-load voltage on the 6 phases through these expressions:

$$\hat{E}_{A_0} = \omega \cdot \frac{d\hat{\Lambda}_A}{d\theta} \tag{3.36}$$

$$\hat{E}_{B_0} = \omega \cdot \frac{d\hat{\Lambda}_B}{d\theta} \tag{3.37}$$

$$\hat{E}_{C_0} = \omega \cdot \frac{d\hat{\Lambda}_C}{d\theta} \tag{3.38}$$

$$\hat{E}_{D_0} = \omega \cdot \frac{d\hat{\Lambda}_D}{d\theta} \tag{3.39}$$

$$\hat{E}_{E_0} = \omega \cdot \frac{d\hat{\Lambda}_E}{d\theta} \tag{3.40}$$

$$\hat{E}_{F_0} = \omega \cdot \frac{d\hat{\Lambda}_F}{d\theta} \tag{3.41}$$

Then, the no-load voltage of the first winding is represented in a graph as a function of the electrical angle.

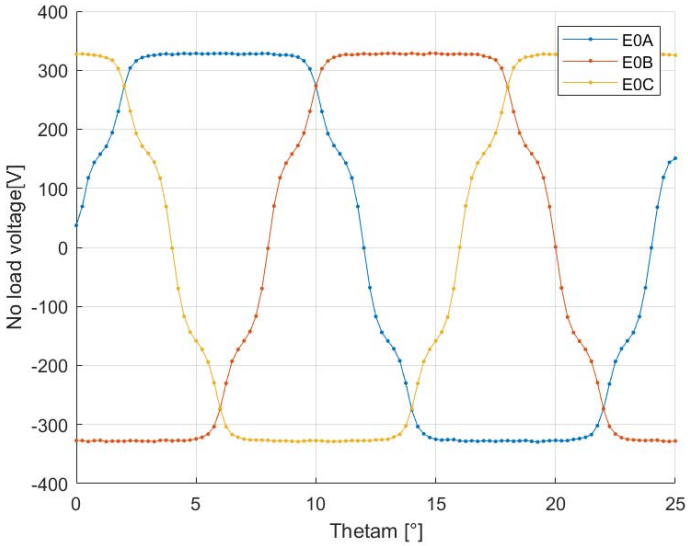

Figure 3.11: Trend of no-load voltage in no-load operation.

Furthermore, considering the flux linkages values in the A-phase computed before, we can calculate the first harmonic through the Fourier's analysis.
After finding the a_h and b_h values it is possible to recreate the starting signal, and thanks to the rotor position chosen we can write:

$$\Lambda_A(\theta_m) = \Lambda_0 + \sum_{h=1}^{N} a_h \cdot cos(h \cdot \omega_1 \cdot t) \tag{3.42}$$

There are only cosine values, as it is represented in the graph (3.12).

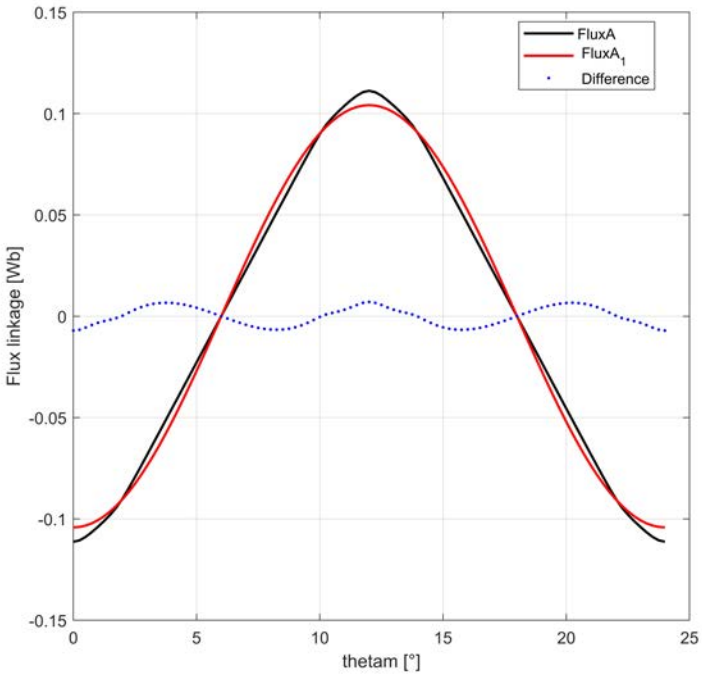

Figure 3.12: Trend of the first harmonic flux linkage in no-load operation.

The blue line shows the difference between the flux and its fundamental. Even if it is small, the no-load voltage results very distorted according to its first harmonic, as this parameter is the flux linkage derivative. In this way, the harmonic content weight is amplified. The formula that is used for the calculus is:

$$e(\theta_m) = -\omega_m \sum_{h=1}^{N} (h \cdot a_h) \cdot sin(h \cdot \omega_1 \cdot t) \tag{3.43}$$

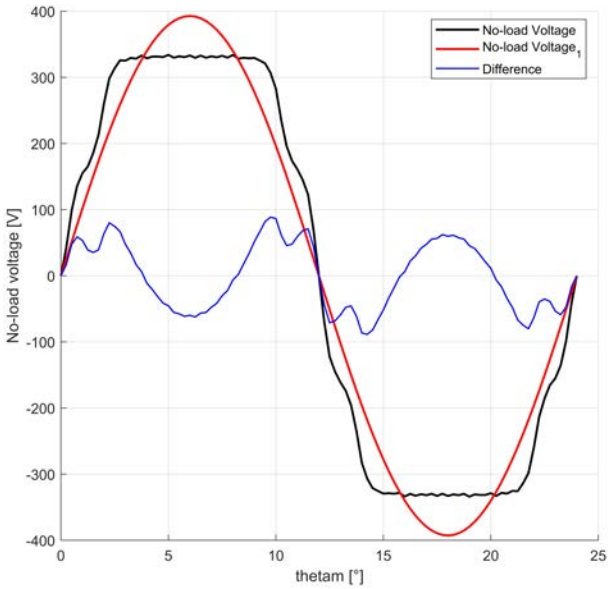

Figure 3.13: Trend of first harmonic no-load voltage in no-load operation.

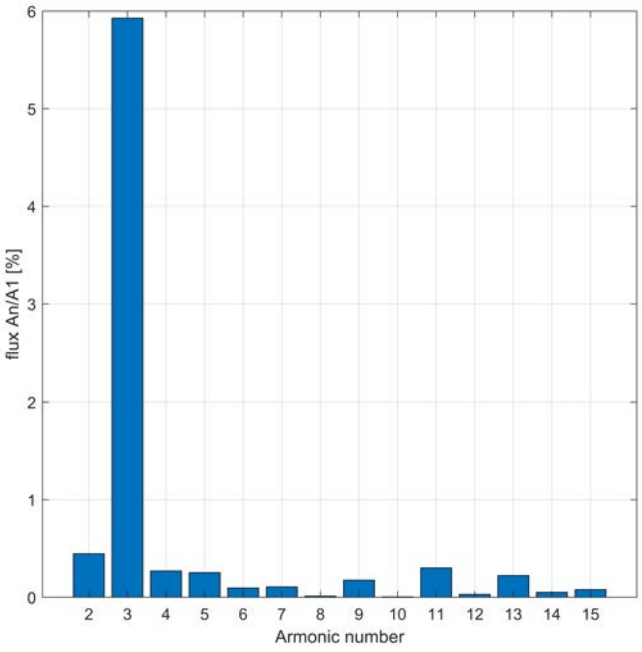

Figure 3.14: Harmonic content of the flux linkage.

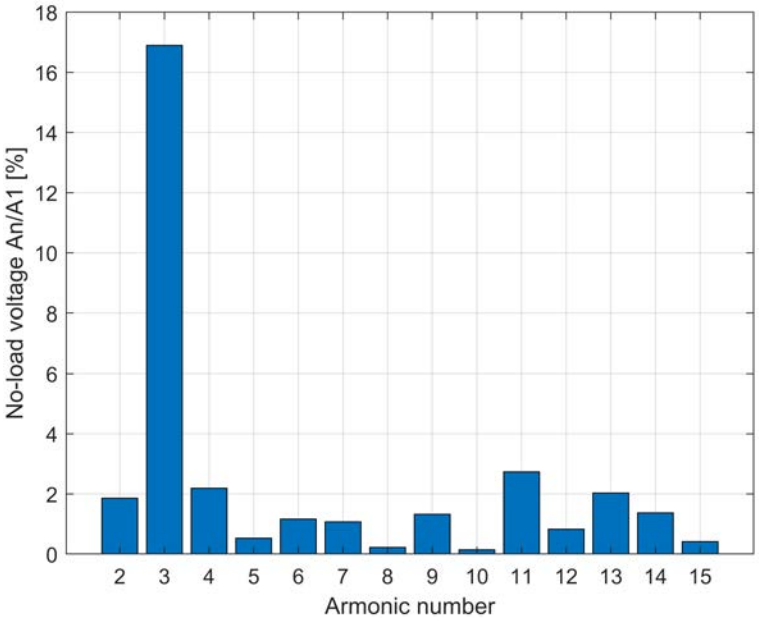

Figure 3.15: Harmonic content of the no-load voltage.

The only prevalent harmonic is the third one. The way to decrease its value is to adopt a specific configuration of the winding (delta or star).
Another important physical quantity in this kind of motor is the cogging torque. This is always present even if the stator current is null. It is possible to evaluate it by turning the rotor and keeping the motor disconnect to the power supply.
This torque is developed by the attractive force that tries to maintain alignment among teeth and permanent magnets: the rotor tends to line up with the maximum number of stator teeth in such a way that the reluctance of a flux line is minimal. This phenomenon is affected by the size and the shape of the magnet and by the geometry of the stator teeth.

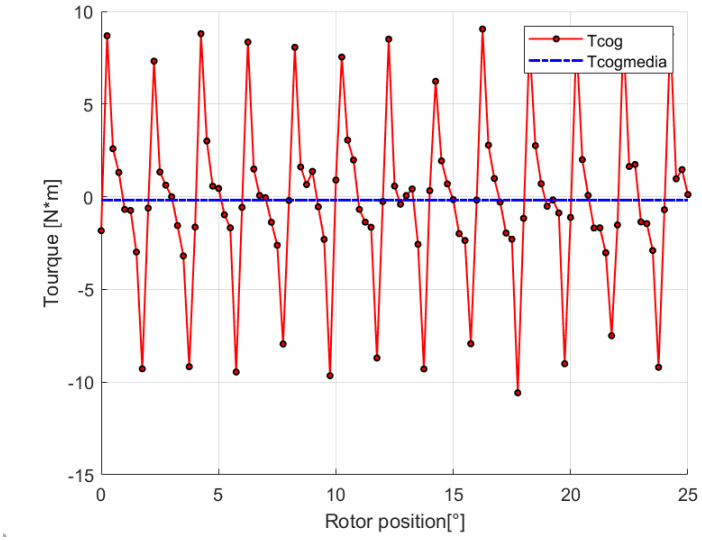

Figure 3.16: Trend of the cogging torque in no-load operation.

As we can see in the graph, it is a type of torque with an average value equal to zero and so it does not contribute to the normal operating of the motor, but it adds to an oscillating component at the constant torque.

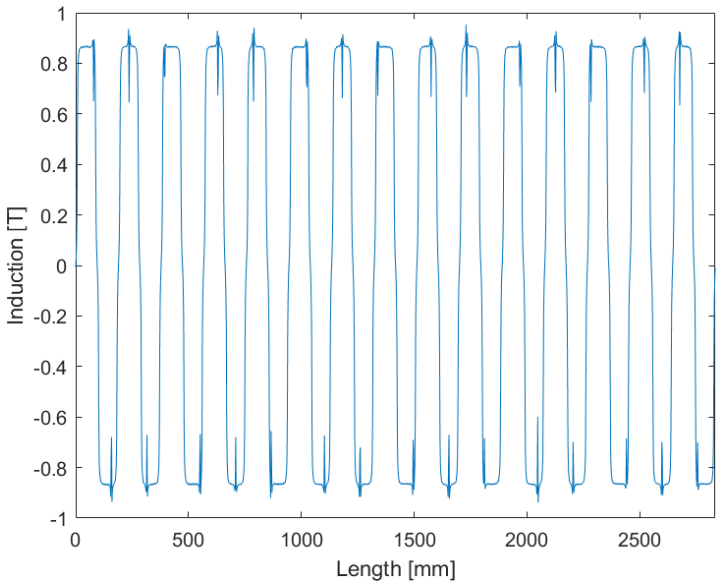

Figure 3.17: Trend of the air-gap induction in no-load operation.

At the end, we reported also the trend of the air-gap induction in picture (3.17). As we can note, the maximum value of induction is equal to the one we calculated in the previous paragraph.
The other operation that we want to analyse with FEMM is the load one.

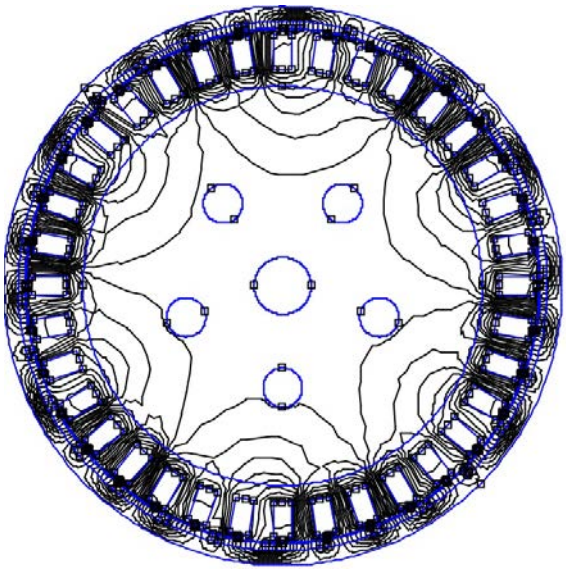

Figure 3.18: Flux lines in load operation.

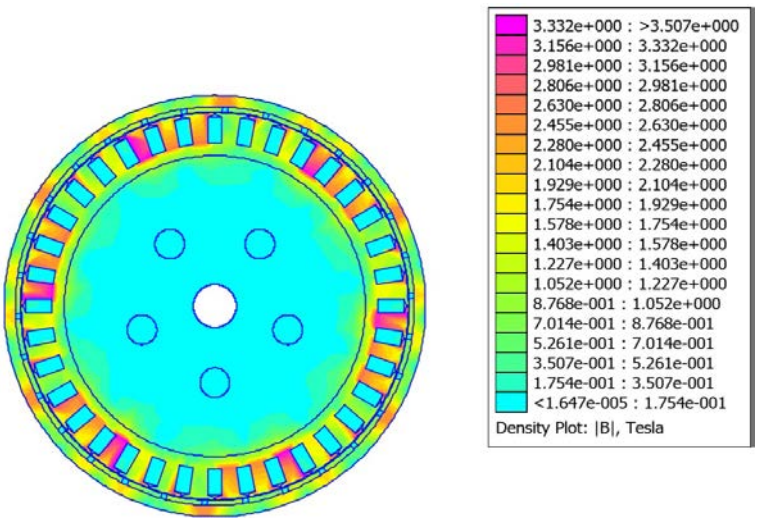

Figure 3.19: Induction density plot for load operation.

In this situation the motor is rotated at load sending in the stator winding the current to have the maximum ratio between torque and current.
For this reason, we have to find the operating point where we have the maximum torque developed per Ampere sent into stator winding, called MTPA (Maximum Torque Per Ampere).
The MTPA search means to research an angle which makes it possible to have the maximum torque given a certain current. It is a matter of determining the angle α_i^e which is the phase angle of the direct and quadrature axis currents.
Thanks to Matlab, imposing the $\hat{I}$ value, the value of the torque through Maxwell stress tensor torque is calculated varying α_i^e angle obtaining the figure (3.20).

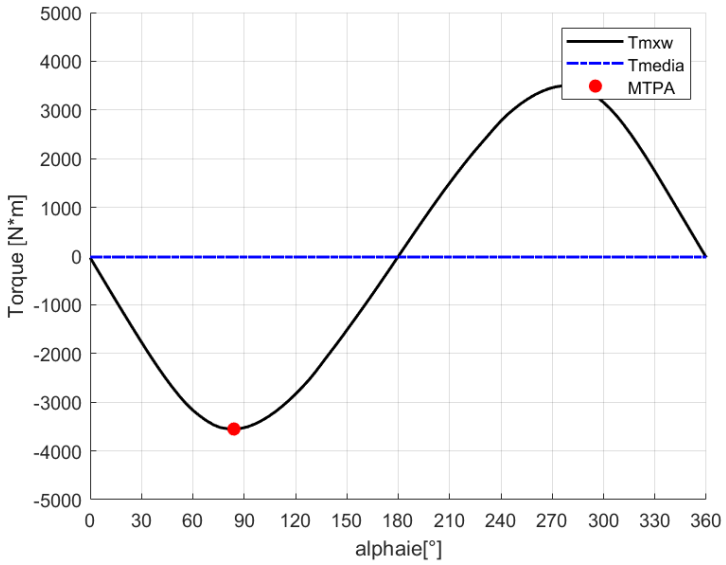

Figure 3.20: MTPA.

From this, we find out that the MTPA is equal to 84°.
At this point it is possible to calculate the value of the torque that the motor is able to provide in MTPA condition.

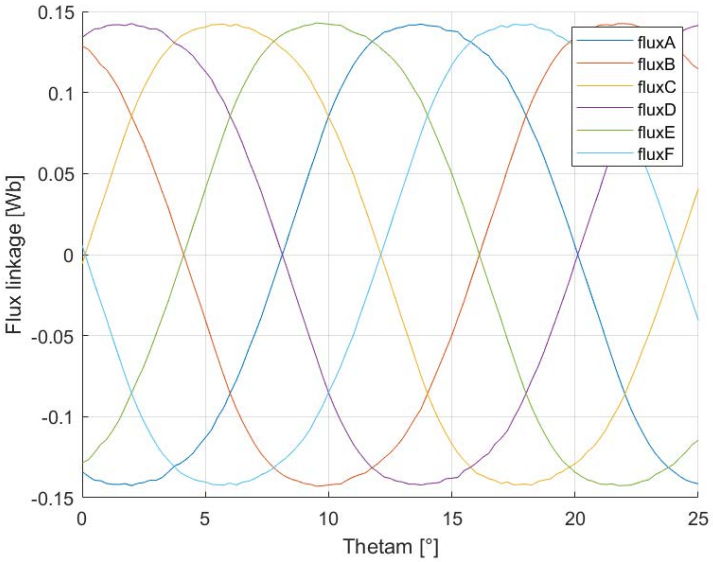

Figure 3.21: Trend of the flux linkage in load operation.

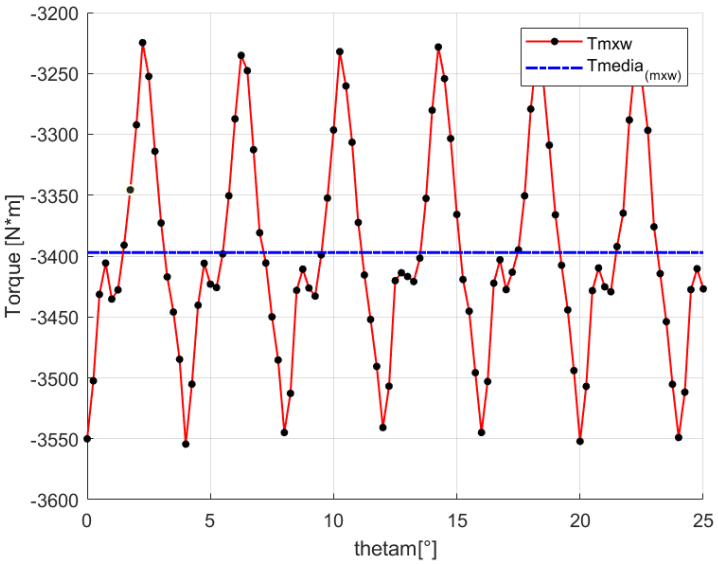

Figure 3.22: Trend of the torque in load operation.

Then, it is reported the torque harmonic analysis computed through the Maxwell tensor stress.

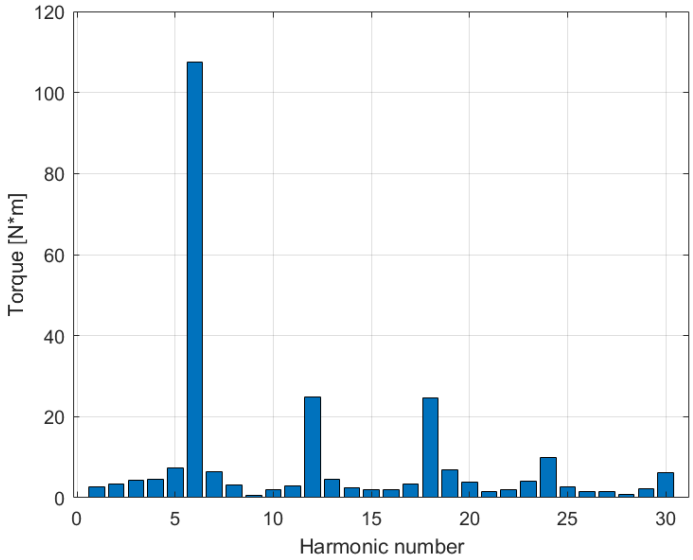

Figure 3.23: Harmonic content of the torque.

It presents a contribution of the sixth, twelfth and eighteenth harmonic, probably due to the fact that is a sub-multiple of the number of slots.
Moreover, we want calculate the MTPA line for different combinations of current values I_d (direct axis current) and I_q (quadrature axis current).
To do this, we have to compute first the flux linkage Λ_d and Λ_q and then the torque value varying I_d and I_q.
In the picture (3.24), we can see:

- Coloured curves. They are the iso-torque curves that indicate for what pairs of I_d and I_q values we obtain the same developed torque value. They are represented with different colours according to the value of the torque numerically reported.
- Black curves. They indicate the maximum current value to obtain that certain torque values.
- Red line. It indicates the MTPA.

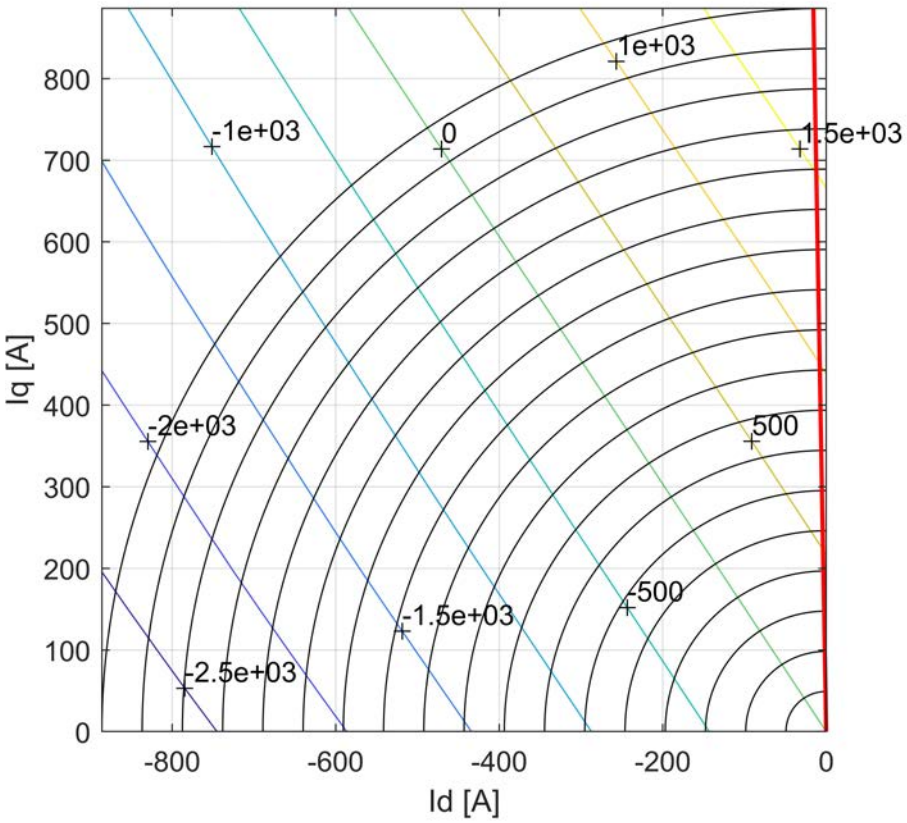

Figure 3.24: Mapping.

3.1.2 SR

A reluctance machine is an electric machine in which torque is produced by the tendency of its moveable part to move to a position where the inductance of the excited winding is maximized (Miller 2001).
The Switched Reluctance Motor presents a double salience, that is, poles are both on the stator and on the rotor, and it differentiates from stepper motor:

- For the less number of stator and rotor poles.
- For the bigger torque developed.
- To have a position sensor
- To have a current control

In this case, a 6/4 SRM is studied, which means that it has 6 poles on the stator (N_{ps}) and 4 on the rotor (N_{pr}), and its data are taken from the paper of Song Shoujun, Liu Weiguo, Dieter Peitsch and Uwe Schaefer.

Physical quantity	**Unity of measurement**	**Value**	**Symbol**
Number of phases		3	m
Rated torque	Nm	12	τ_m
Rated speed	rpm	2827.43	Ω
Rated voltage	V	270	V_n
Rated current	A_{rms}	25	I_{rms}
Frequency	Hz	400	f

Table 3.4: Switched reluctance motor data. (Data source: Shoujun et al. 2010)

Geometrical data

Physical quantity	Unity of measurement	Value	Symbol
Internal stator diameter	mm	130	D_{si}
External stator diameter	mm	160	D_{se}
External rotor diameter	mm	60	D_{re}
Shaft diameter	mm	30	D_{sh}
Stack length	mm	80	L_{stk}
Length of the end-turn	mm	50.184	L_{oh}
Overall length	mm	130.184	L_e
Airgap height	mm	0.4	g
Stator poles arc	°	30	β_s
Stator poles height	mm	24.6	h_s
Stator poles width	mm	20.91	w_s
Rotor poles arc	°	32	β_r
Rotor poles height	mm	10	h_r
Rotor poles width	mm	22.05	w_r

Table 3.5: Switched reluctance motor geometrical data. (Data source: Shoujun et al. 2010)

In addition to this, rotor and stator sheets are made of M270-35A, for which we consider also the saturation. For this reason, B-H curve of this material is reported:

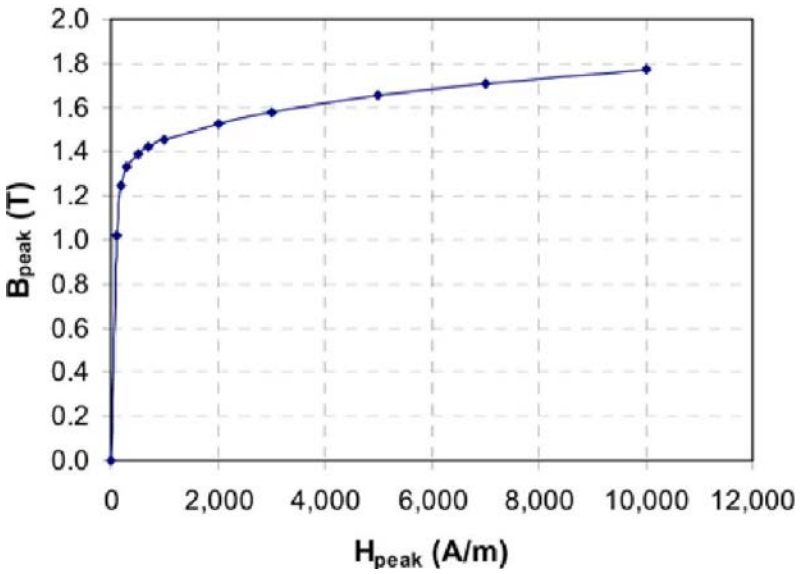

Figure 3.25: M270-35A B-H characteristic. (Source: Gao et al. 2010)

The shaft is made of mild steel and we report below its the B-H characteristic:

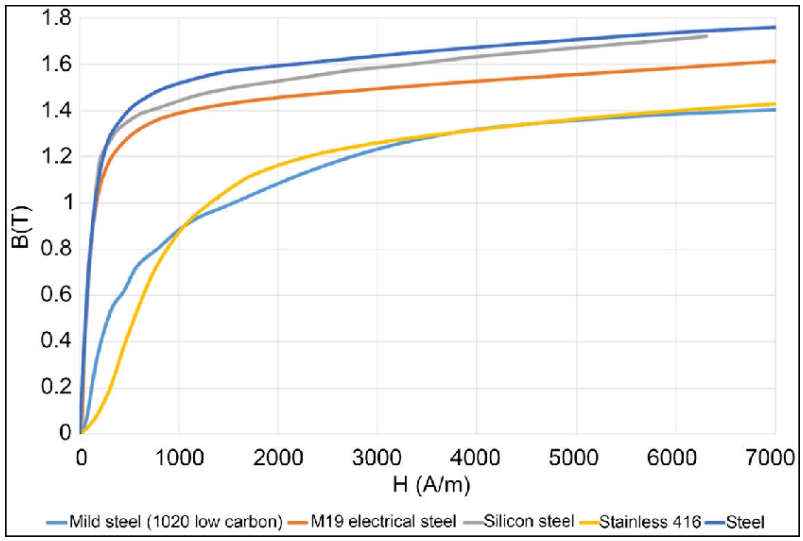

Figure 3.26: Mild steel B-H characteristic. (Source: Kappatou, Zalokostas, and Spyratos 2016)

Winding

It is assumed in the paper that N_p turns wound equal to 12 around each stator pole and the windings on opposite stator poles are connected in series to form a phase.

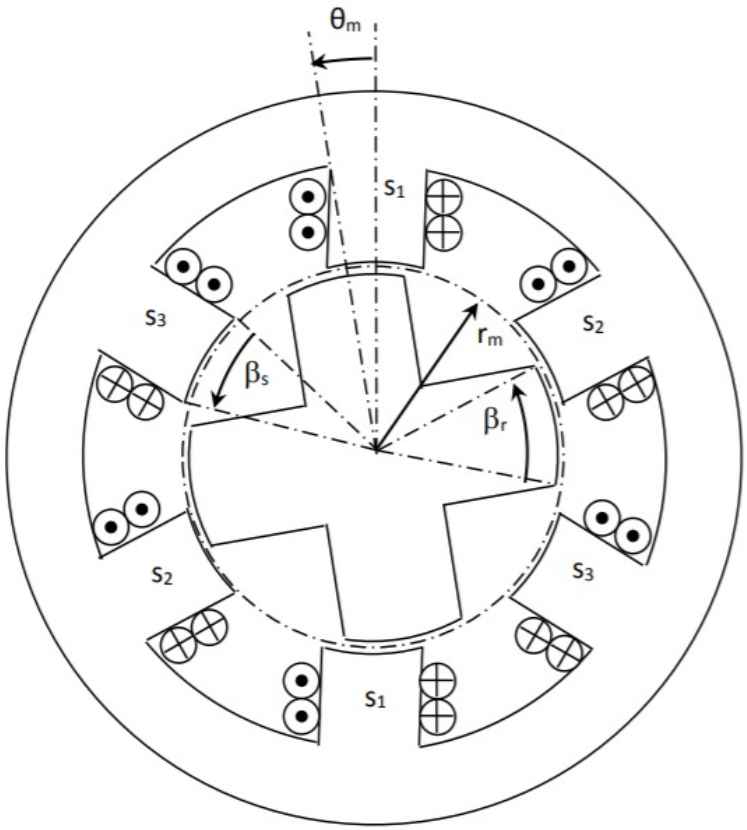

Figure 3.27: Configuration of the winding. (Source: Gallo 2015)

Operation

Conversely to the permanent magnet motor, it is difficult to describe the operation of this machine, because it works in the saturation part of the B-H characteristic. To understand the results which will be reported, we explain its functioning starting from the linear analysis.

Before beginning, we have to make some assumptions:

- The inductance is not a function of current, as it is working in the linear part of the B-H characteristic.
- The fringing flux is ignored, so it presents only the radial component of the flux in the air-gap.

The mutual coupling among the phases is null or very small, therefore it is not considered. The voltage equation referring to only one phase is:

$$v = R \cdot i + \frac{d\phi}{dt} = R \cdot i + \omega_m \cdot \frac{d\phi}{d\theta} = R \cdot i + \omega_m \cdot \frac{d(L \cdot i)}{d\theta}$$
$$= R \cdot i + L \cdot \frac{di}{dt} + \omega_m \cdot i \cdot \frac{dL}{d\theta} \tag{3.44}$$

So, the instantaneous electrical power is:

$$vi = R \cdot i^2 + L \cdot i \cdot \frac{di}{dt} + \omega_m \cdot i^2 \cdot \frac{dL}{d\theta} \tag{3.45}$$

while the rate of change of magnetic stored energy at any instant is:

$$\frac{d}{dt} \cdot (\frac{1}{2} \cdot L \cdot i^2) = L \cdot i \frac{di}{dt} + \frac{1}{2} \cdot i^2 \cdot \frac{dL}{dt} \tag{3.46}$$

The mechanical power conversion, thanks to the law of conversion energy, is:

$$p = \omega_m \cdot T_e \tag{3.47}$$

Thus we can write:

$$T_e = \frac{1}{2} \cdot i^2 \cdot \frac{dL}{d\theta} \tag{3.48}$$

If this motor worked magnetically linear, it would have a low energy ratio and it would make poor utilization of the drive.
For this reason, it is necessary to briefly explain the saturation operation. It differs from the linear operation because W_f (stored magnetic energy) and W_c (co-energy) are not equal. In fact, the effect of the saturation is that $W_f < W_c$.
Taking a generic displacement angle $\Delta\theta$, the energy exchanged with the supply is:

$$\Delta W_e = \int e \cdot i \cdot dt = \int i \cdot \frac{d\phi}{dt} \cdot dt = \int i \cdot d\phi \tag{3.49}$$

Therefore, the mechanical work is:

$$\Delta W_m = \Delta W_e - \Delta W_f \tag{3.50}$$

and this is equated to $T_e \Delta\theta$, in the limit when $\Delta\theta \to 0$:

$$T_e = \left[\frac{\partial W_c}{\partial \theta}\right]_{i=const} \tag{3.51}$$

FEMM analysis

As there is not any mutual coupling among the phases, they can be analysed independently. In particular we can consider only a phase and then the results can be extended to the other phases considering the displacement angle.
The analysis is done for the whole motor, because of the asymmetry between stator and rotor.
As regard to the discretization of the domain, the region in correspondence with the air-gap is that one where the field presents a higher gradient. Therefore, the mesh has to be denser. If it is not, it could be a problem to calculate the torque with Maxwell stress tensor because of the irregular and discontinuous trend of the tangential induction component computed with the finite element method.
Furthermore, in steady-state working conditions, the motor works with strongly saturated magnetic circuit sections. Consequently, it is necessary to have a dense mesh for the stator and rotor poles too in order to guarantee accurate results.
The figure (3.28) shows the set mesh and the geometry of the motor for this study.

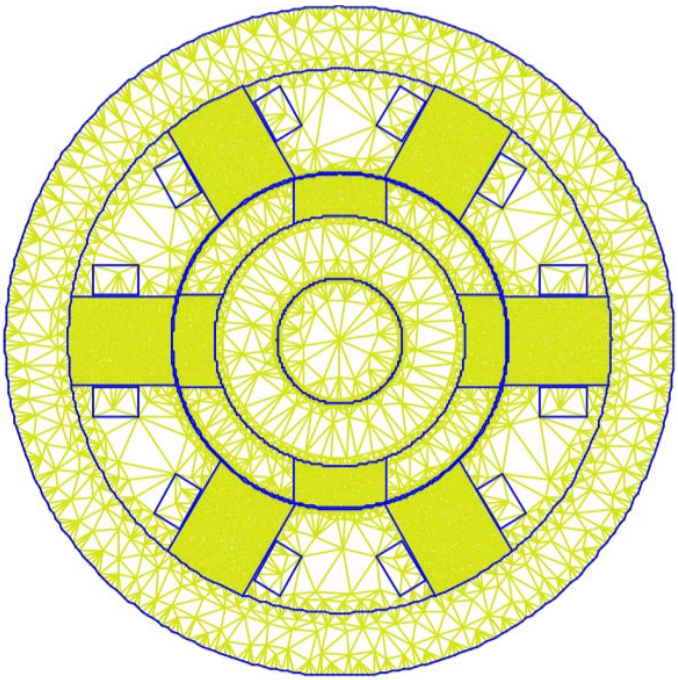

Figure 3.28: Geometry of the motor.

So we can start the load analysis, as this machine doesn't work in no load operation.
Before starting the analysis, we will report the solution of flux and induction developed by FEMM supplying only the A-phase, as we said earlier.
Then we will calculate the most important parameters for this machine: the flux linkage, the co-energy and the torque. This values, as reported in the equations of the previous paragraph, are functions of the rotor angle.
In figure (3.29) and (3.30) it is shown the case where the supplied stator poles are aligned with the rotor ones.

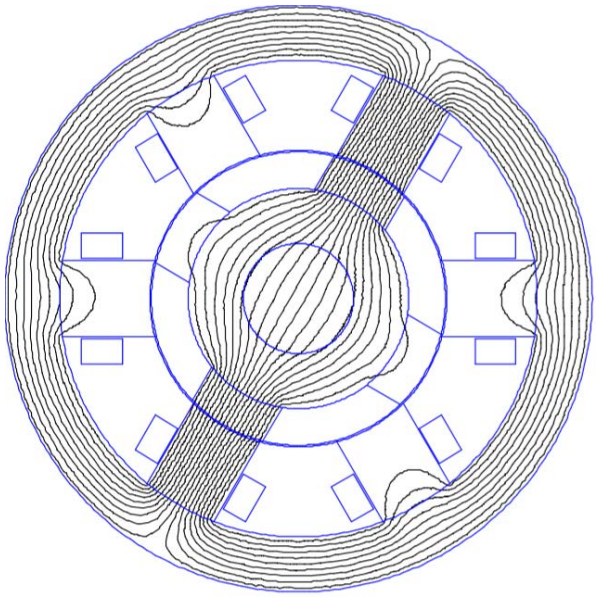

Figure 3.29: Trend of flux lines supplying only A-phase in aligning condition.

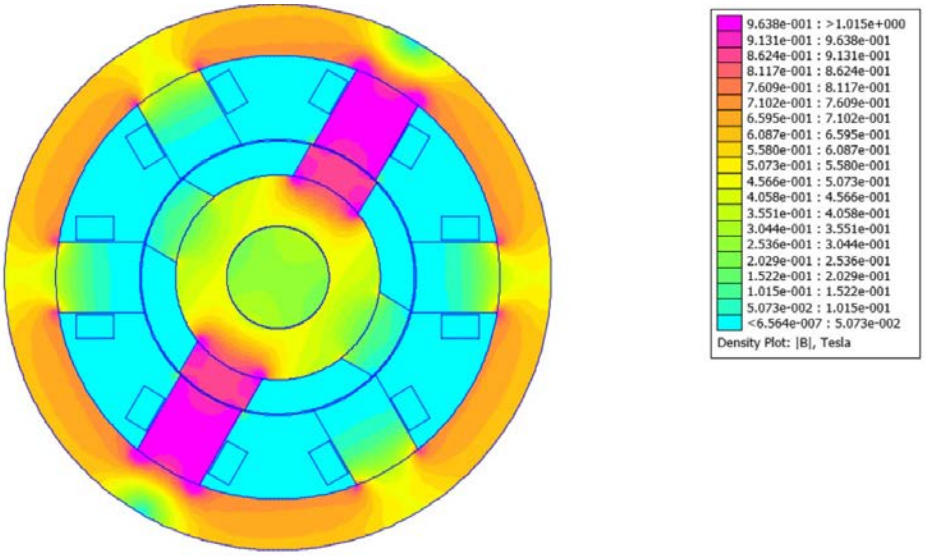

Figure 3.30: Density plot of the induction supplying only A-phase in aligning condition.

The reported figures (3.31), (3.32) and (3.33) show the trend of the main characteristic of this motor varying the input current.

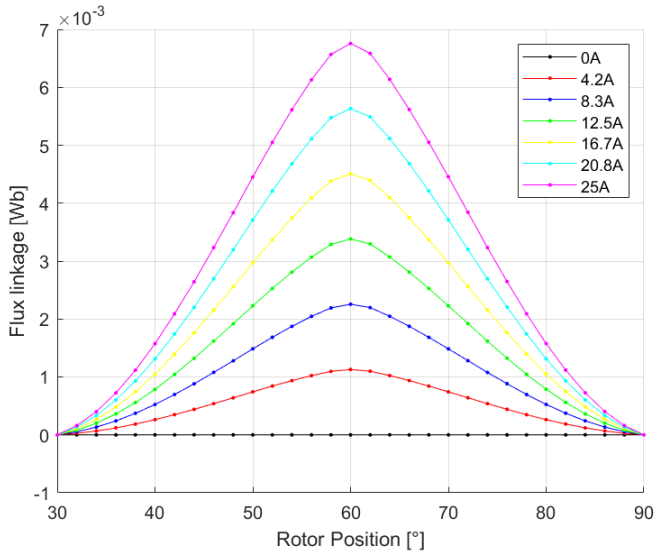

Figure 3.31: Trend of flux linkage in function of the rotor position varying the input current.

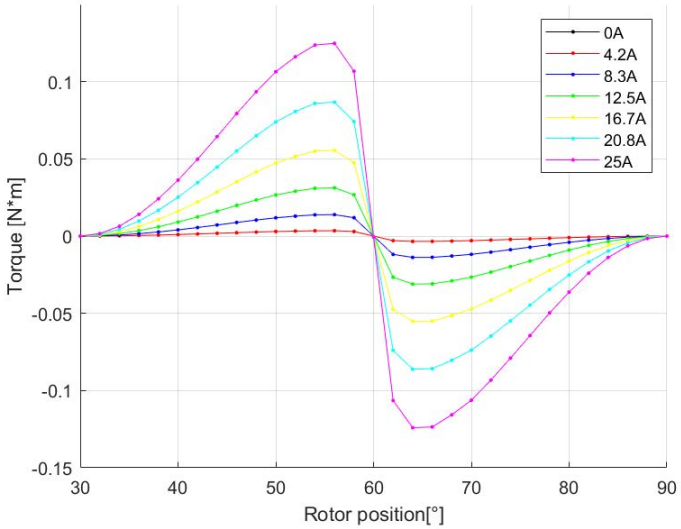

Figure 3.32: Trend of torque in function of the rotor position varying the input current.

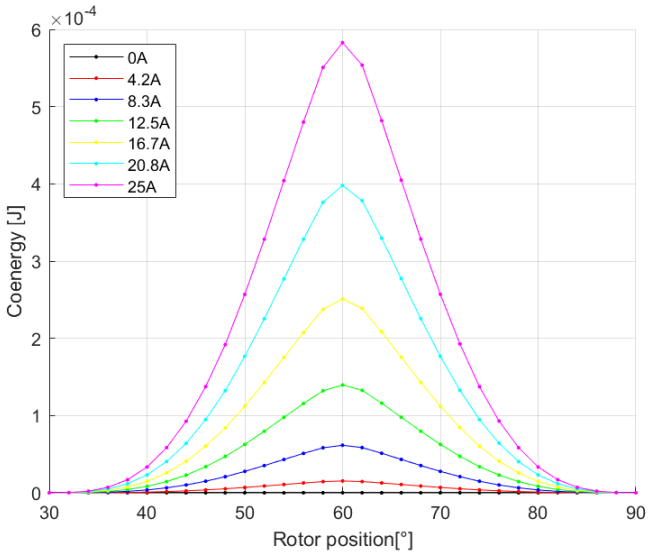

Figure 3.33: Trend of co-energy in function of the rotor position varying the input current.

As we can note, we have a defined operating area between 30° and 90°.
The positive motoring torque is developed only when there is an increase of inductance, that is, until the rotor poles are aligned with the stator ones. In this case it occurs between 30° and 60°. At 30°, the leading edge of the rotor pole is aligned with the first edge of a stator one; at 60° the poles are fully aligned.
After this point, as we can see in figure (3.32), the torque changes direction, due to the attractive force that produces a retarding torque. Therefore, if the motor was fed with a constant current, the average torque in a cycle would be zero. For this reason, the current is switched off after it is reached the peak of positive torque.
Evidently, the production of continuous torque requires that all the other phases are fed too.
At the end, it is also reported the trend of the air-gap. The figure (3.34) shows the normal component, instead the figure (3.35) the tangential one. We can note the oscillating trend of this latter component and for this reason the computed torque presents a strong sensitivity towards the set mesh.

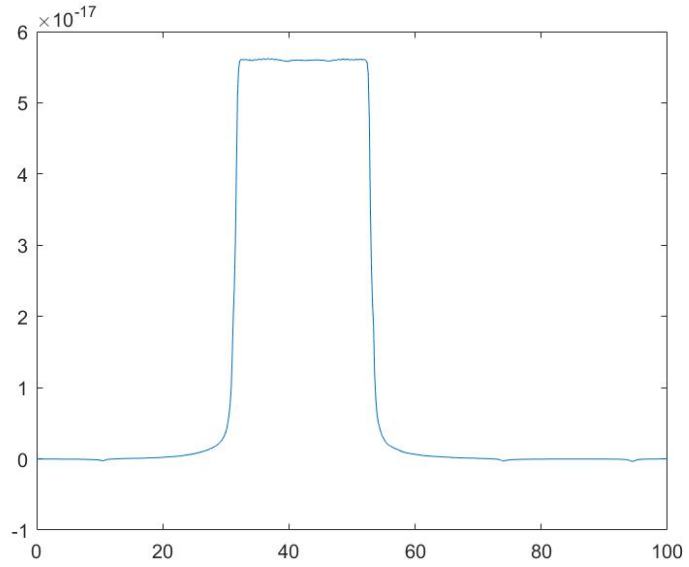

Figure 3.34: Trend of the normal component of the air-gap induction.

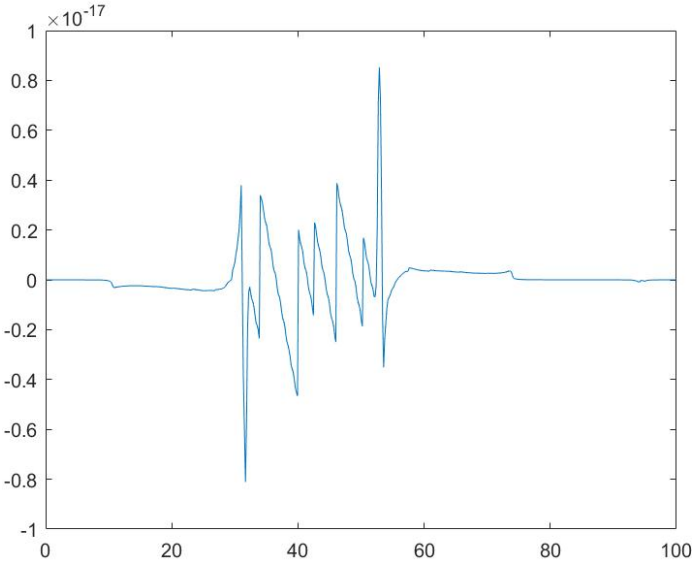

Figure 3.35: Trend of the tangential component of the air-gap induction.

Chapter 4

Thermal analysis

In the electrical machine the electrical and mechanical energy production is always associated with winding and iron losses, as well as friction in case there is movement. The dissipated energy is converted into heat. Part of this energy is collected in some areas of the motor; the rest crosses the motor towards the outer surface where there is a fluid (cooler than the surface) to refrigerate it.
We can recognise three types of transfer of heat:

- Conduction. It is the transfer of internal energy through microscopic collisions of particles and movement of electrons within the body.
- Convection. It is the transfer of heat through a macroscopic movement of fluid particles.
- Radiation. The heat is transferred by electromagnetic waves.

They usually happen simultaneously even though one is often predominant over the others, which can be ignored.
The more electrical engine (MEE) aims to mount the electrical generators in a hotter part of the engine. By doing so, the number of gearboxes in the system can be reduced increasing the efficiency and reliability of the whole system. In this case, the electrical machine needs to withstand the extreme environment of a gas turbine engine (Fang et al. 2013).

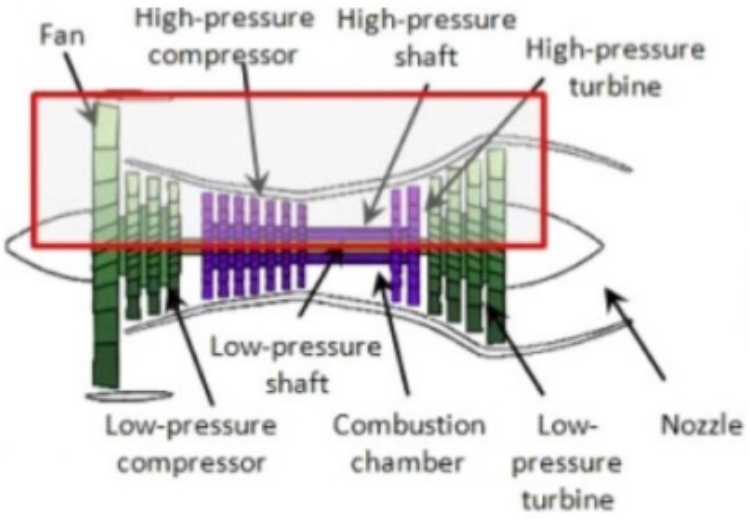

Figure 4.1: Placement of the electrical motor in a more electrical aircraft. (Source: Cavagnino et al. 2013)

In this way, the electrical machine is located near the turbine at around $350°C$, to which the winding temperature is added. The insulation system should, therefore, withstand a peak temperature of $500°C$, but it could be higher under certain contingency situations.
In this paragraph, we will focus on the losses of the two motors and on the developed temperature.

4.1 Motors

4.1.1 PMAC

First of all, we will compute the losses in the various parts of the motor.
The copper losses are:

$$P_{cu_{tot}} = m \cdot R_{75°C} \cdot I^2 \tag{4.1}$$

where $R_{75°C}$ is the phase resistance reported to the operating temperature. The paper from where we took the data gives us the phase resistance at 20°C, that is 16mΩ. Using the formula $R_{75°C} = R_{20°C} \cdot [1 + \alpha \cdot (T_2 - T_1)]$, we obtain that $R_{75°C}$ is equal to 19.84mΩ.
Therefore, thanks to the equation (4.1), we can compute P_{cu} as follows:

$$P_{cu_{tot}} = 6 \cdot 19 \cdot 10^{-3} \cdot 443^2 = 23.3kW$$

Before computing the iron losses, we have to see the specific iron losses of strip material (for cobalt-iron alloy: $p_{fe_{rif}}$=1.5 W/kg at B_{rif}=1.5 T and f_{rif}=50 Hz) and the peak induction value in the teeth ($\hat{B_T} = 3.42T$), and in the stator and rotor yoke (respectively $\hat{B_{ys}} = 1.788T$ and $\hat{B_{yr}} = 0.947T$) from the previous chapter analysis.
Then, we have to report the specific iron losses of the strip material to the operating induction and frequency using the previous value:

$$p_{spec_T} = p_{fe_{rif}} \cdot k_{hys} \cdot \left(\frac{f_n}{f_{rif}}\right) \cdot \left(\frac{\hat{B_T}}{B_{rif}}\right)^2 + p_{fe_{rif}} \cdot k_{cp} \cdot \left(\frac{f_n}{f_{rif}}\right)^2 \cdot \left(\frac{\hat{B_T}}{B_{rif}}\right)^2 \quad (4.2)$$

where k_{hys} and k_{cp} are two coefficients that take into account the hysteresis and the eddy current losses.
Substituting the numbers in the equation (4.2), we obtain the specific losses for the teeth:

$$p_{spec_T} = 1.5 \cdot 0.85 \cdot \left(\frac{600}{50}\right) \cdot \left(\frac{3.42}{1.5}\right)^2 + 1.5 \cdot 0.15 \cdot \left(\frac{600}{50}\right)^2 \cdot \left(\frac{3.42}{1.5}\right)^2 = 260W/kg$$

After this, we have to compute the weight of this part of the motor, knowing that the cobalt-iron alloy's density is γ_{cia}=8.12 g/cm^3:

$$G_T = \gamma_{cia} \cdot Q \cdot h_s \cdot w_t \cdot L_{stk} \quad (4.3)$$

So:

$$G_T = 8.12 \cdot 10^{-3} \cdot 36 \cdot 6.19 \cdot 3.34 \cdot 7 = 42.31kg$$

Due to the production, the iron losses have to be raised. This increase is taken into account by the coefficient k_{magg}, that is between 1.5 and 2. We assume that

it is 1.5 and finally we can calculate the iron losses in the teeth:

$$P_{iron_T} = k_{magg} \cdot G_T \cdot p_{spec_T} \tag{4.4}$$

that are equal to:

$$P_{iron_T} = 1.5 \cdot 42.31 \cdot 260 = 16500W = 16.5kW$$

Going on with the study, we can compute the other iron losses using the same procedure starting from the stator one.
The specific losses in the front part of the slots are:

$$p_{spec_{FI}} = 1.5 \cdot 0.85 \cdot \left(\frac{600}{50}\right) \cdot \left(\frac{1.788}{1.5}\right)^2 + 1.5 \cdot 0.15 \cdot \left(\frac{600}{50}\right)^2 \cdot \left(\frac{1.788}{1.5}\right)^2 = 67.8W/kg$$

While its weight is:

$$G_{FI} = \gamma_{cia} \cdot \pi(\frac{D_{si}^2}{4} - \frac{D_{sft}^2}{4}) \cdot L_{stk} \tag{4.5}$$

$$= 8.12 \cdot 10^{-3} \cdot \pi(\frac{70^2}{4} - \frac{10^2}{4}) \cdot 7 = 214.3kg$$

Thanks to the equation (4.4):

$$P_{FI} = 1.5 \cdot 67.8 \cdot 214.3 = 21786W = 21.8kW \tag{4.6}$$

At the end, we compute also the iron losses in the rotor yoke always starting from the specific iron losses:

$$p_{spec_{BI}} = 1.5 \cdot 0.85 \cdot \left(\frac{600}{50}\right) \cdot \left(\frac{0.947}{1.5}\right)^2 + 1.5 \cdot 0.15 \cdot \left(\frac{600}{50}\right)^2 \cdot \left(\frac{0.947}{1.5}\right)^2 = 19W/kg$$

After that, we calculate its weight:

$$G_{FI} = \gamma_{cia} \cdot \pi(\frac{D_{re}^2}{4} - \frac{(D_{ri} + 2 \cdot tm)^2}{4}) \cdot L_{stk} \tag{4.7}$$

$$= 8.12 \cdot 10^{-3} \cdot \pi(\frac{98.04^2}{4} - \frac{(90.4 + 2 \cdot 1.2)^2}{4}) \cdot 7 = 83.4kg$$

So, for equation (4.4):

$$P_{BI} = 1.5 \cdot 19 \cdot 83.4 = 2376.5W = 2.4kW$$

At the end, we can compute the mechanical losses through an empirical formula:

$$P_{mecc} = 0.3 \cdot P_{n_{[kW]}} \cdot \sqrt{\Omega_{[rpm]}} \tag{4.8}$$

$$= 0.3 \cdot 301.6 \cdot \sqrt{2400} = 4433W = 4.4kW$$

After calculating the losses in the motor, we have to check if the heat is acceptable. To do this we use the FEMM *heat flow problem* with the same geometry that we used for the magnetic ones except for the insulation around the winding in the slots.
Initially, we have to set again the materials with their thermal conductivity ($\frac{W}{m \cdot K}$). For the insulation material we hypothesize that it is a polymeric ceramic with a linear thermal conductivity of $0.5\frac{W}{m \cdot K}$ and a thickness of 0.5 mm.
Furthermore, we suppose that the heat coming from the losses is generated by the material. Therefore, we have to determine also the volume heat generation for each material by calculating its volume.
After this, we have to define the convection system of the motor.
For the paper at issue, the electrical machine is supposed to be cooled by air axially flowing through the air-gap, due to the high axial air flow during the turbofan operation. We left the holes in the middle of the motor, even if they were projected only for the prototype version, in order to have cooler temperature inside.
In addition to the settings done before, we have to set two types of boundary conditions. Firstly, we have the heat flux boundary condition as the source of heat produced by generator losses for the mechanical losses in the middle of the air-gap. Secondly, the convection boundary condition which is applied to the area in contact with the ambient temperature.
We intended this type of cooling as if it was forced air cooling, so we chose 500 W/(m^2·K) as heat transfer coefficient.
For the figure (4.2) it is not taken into account the ambient temperature, but the displayed temperature represents the over-temperature that the material has to withstand.

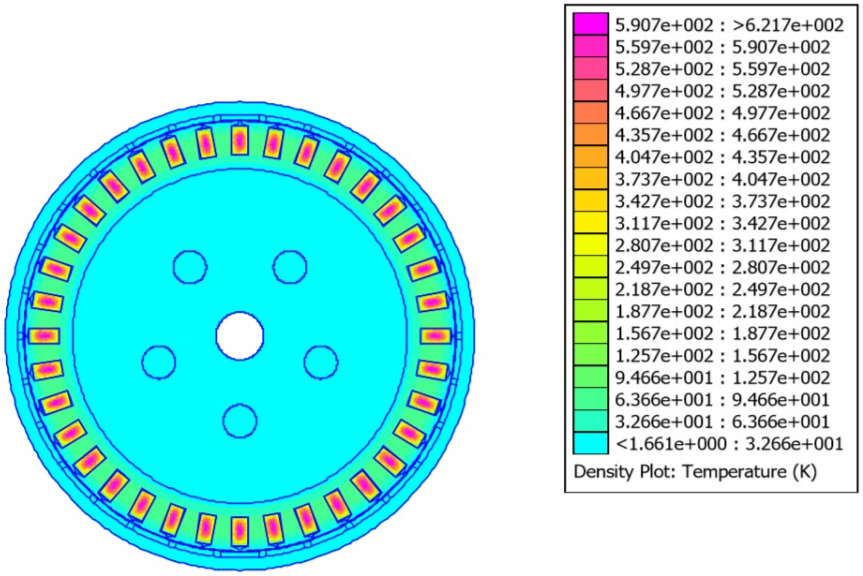

Figure 4.2: Trend of the temperature inside the motor.

As we can see, the over-temperature in the stator winding has a peak of around 500°C, but on average it is around 300°C. So, considering also the ambient temperature, the insulation material has to withstand a peak temperature of around 550°C.
To understand better the state, we report also the detailed situation of a slot.

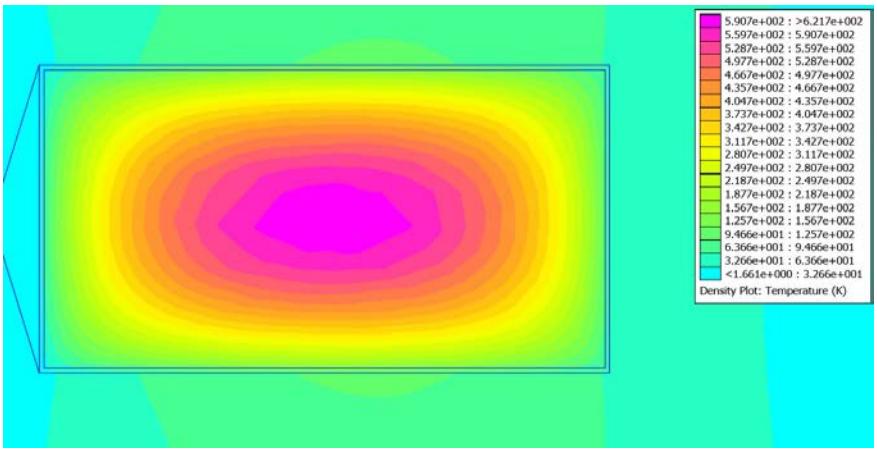

Figure 4.3: Trend of the temperature inside the slot.

We have to consider only the average temperature because we do not know the arrangement of the winding inside the slot.

4.1.2 SR

For this study, it is taken into account the case in which the stator and rotor poles of the C-phase are aligned. This is because we find the maximum value of the induction and therefore we have more iron losses. We have to calculate again the same parameters as before starting from the copper losses:

$$P_{cu,tot} = 3 \cdot 1.2 \cdot 25^2 = 2250W = 2.25kW$$

After that, we have to compute the iron losses, but first of all we have to check the specific iron losses of strip material (for M270-35A: $p_{fe_{rif}}$=1.1 W/kg at B_{rif}=1 T and f_{rif}=50 Hz), the peak induction value in the stator and rotor poles ($\hat{B_{ps}}$=1.757 T and $\hat{B_{pr}}$=1.645 T respectively) and in the stator and rotor yokes ($\hat{B_{ys}}$=1.5 T and $\hat{B_{yr}}$=1.453 T respectively). This values are taken from the case where all the phases are supplied and not only one as in the previous analysis.
After that, we report the values to the operating condition starting from the stator poles:

$$p_{spec_{ps}} = p_{fe_{rif}} \cdot k_{hys} \cdot \left(\frac{f}{f_{rif}}\right) \cdot \left(\frac{\hat{B_{ps}}}{B_{rif}}\right)^2 + p_{fe_{rif}} \cdot k_{cp} \cdot \left(\frac{f}{f_{rif}}\right)^2 \cdot \left(\frac{\hat{B_{ps}}}{B_{rif}}\right)^2$$

$$= 1.5 \cdot 0.85 \cdot \left(\frac{400}{50}\right) \cdot \left(\frac{1.757}{1}\right)^2 + 1.5 \cdot 0.15 \cdot \left(\frac{400}{50}\right)^2 \cdot \left(\frac{1.757}{1}\right)^2 = 55.7W/kg$$

as well as their weight, knowing that the M270-35A material has a density equal to 7.65 kg/dm^3:

$$G_{ps} = \gamma_{M270-35A} \cdot w_s \cdot h_s \cdot N_{ps} \cdot Lstk = 7.65 \cdot 0.2191 \cdot 0.246 \cdot 6 \cdot 0.8 = 1.938kg$$

So, the iron losses for this part is:

$$P_{ps} = k_{magg} \cdot G_{ps} \cdot p_{spec_{ps}} = 1.5 \cdot 1.938 \cdot 55.77 = 161.9W = 0.161kW$$

Going on with the stator part:

$$p_{spec_{ys}} = 1.5 \cdot 0.85 \cdot \left(\frac{400}{50}\right) \cdot \left(\frac{1.51}{1}\right)^2 + 1.5 \cdot 0.15 \cdot \left(\frac{400}{50}\right)^2 \cdot \left(\frac{1.51}{1}\right)^2 = 41.13 W/kg$$

and the stator yoke's weight is:

$$G_{ys} = \gamma_{M270-35A} \cdot \pi \cdot (\frac{D_{se}^2}{4} - \frac{D_{si}^2}{4}) \cdot Lstk = 7.65 \cdot \pi \cdot (\frac{1.6^2}{4} - \frac{1.3^2}{4}) \cdot 0.8 = 1.938 kg$$

Therefore:

$$P_{ys} = 1.5 \cdot 41.13 \cdot 1.938 = 258 W = 0.258 kW$$

Now, we have to repeat the same procedure for the rotor. In fact, starting from the poles:

$$p_{spec_{pr}} = 1.5 \cdot 0.85 \cdot \left(\frac{400}{50}\right) \cdot \left(\frac{1.645}{1}\right)^2 + 1.5 \cdot 0.15 \cdot \left(\frac{400}{50}\right)^2 \cdot \left(\frac{1.645}{1}\right)^2 = 48.82 W/kg$$

and their weight is:

$$G_{pr} = \gamma_{M270-35A} \cdot w_r \cdot h_r \cdot N_{pr} \cdot Lstk = 7.65 \cdot 0.2205 \cdot 0.1 \cdot 4 \cdot 0.8 = 0.59 kg$$

So that:

$$P_{pr} = 1.5 \cdot 48.82 \cdot 0.59 = 43.2 W = 0.0432 kW$$

As before, we calculate also the rotor yoke losses as follows:

$$p_{spec_{yr}} = 1.5 \cdot 0.85 \cdot \left(\frac{400}{50}\right) \cdot \left(\frac{1.453}{1}\right)^2 + 1.5 \cdot 0.15 \cdot \left(\frac{400}{50}\right)^2 \cdot \left(\frac{1.453}{1}\right)^2 = 38.02 W/kg$$

and its weight:

$$G_{yr} = \gamma_{M270-35A} \cdot \pi \cdot (\frac{D_{re}^2}{4} - \frac{D_{ri}^2}{4}) \cdot Lstk = 7.65 \cdot \pi \cdot (\frac{0.6^2}{4} - \frac{0.3^2}{4}) \cdot 0.8 = 1.3 kg$$

Therefore, we obtain:

$$P_{yr} = 1.5 \cdot 38.02 \cdot 1.3 = 74.14 W = 0.0741 kW$$

We don't consider the losses in the shaft as they would be very small and so negligible.

To complete the analysis of this motor, we have calculate the mechanical losses, too.

Obtained from the complete analysis (feeding all the phases of the motor) the rated torque equal to τ_N=12 N·m, and being the speed, for which we have the peak of torque, Ω_m=12000 r/min (1256.64 rad/s), we can compute the developed active power through:

$$P_n = \tau_N \cdot \Omega_m = 12 \cdot 1256.64 = 15896W = 15.9kW \tag{4.9}$$

Therefore for the equation (4.8):

$$P_{mecc} = 0.3 \cdot 15.9 \cdot \sqrt{12000} = 522.5W$$

Consequently, adopting the same geometry with the addition of the insulation material used also for the permanent magnet machine, we want to verify if the heat in motor is acceptable using FEMM.

For the paper in question, the electrical machine is cooled by a forced water system composed by six water channels arranged beyond the external diameter of the motor.

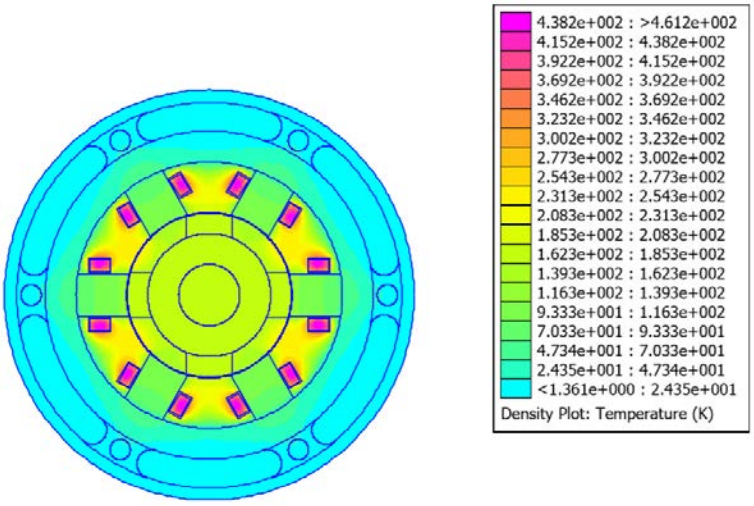

Figure 4.4: Trend of the temperature inside the motor.

Even in this case, we don't consider the ambient temperature, but only the over-temperature that the machine has to withstand. Therefore we can note that there

is a peak of around 500°C in the stator winding, but on average we have 350°C. As before, we report also a focus of the winding.

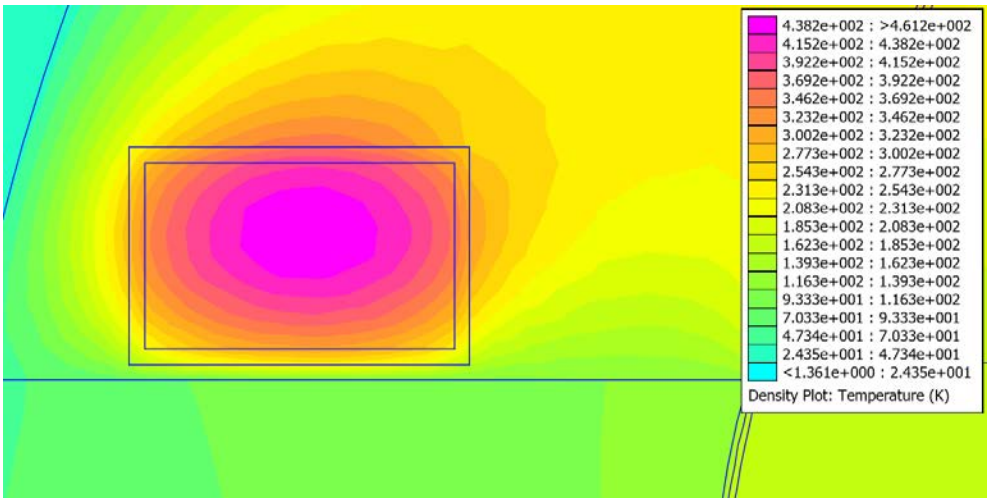

Figure 4.5: Trend of the temperature inside the motor.

Also in this case, we consider only the average over-temperature, because we don't know the arrangement of the winding around the pole.

Chapter 5

Thermal Insulation

Traditional electrical generators used today on aircraft operate at 115 Vac. They, therefore, don't provide sufficient power for the newest aircraft for MEA, as the electrical power demand is increasing. It is necessary to increase the current or the voltage to satisfy the difference requirement. A higher voltage is chosen, because in this way the equipment weight is controlled, but it could develop partial discharge in the insulation system. This phenomenon is more frequent in low pressure operating environment where the airplane works than under normal operating conditions. It also causes the damage of the insulated material increase. For the air resistance given by the air density, a turboprop aircraft usually flies at about 6000 meters high. This is a good compromise between power decrease (as there is less oxygen) and fuel consumption to maintain the same speed. The jet engine aircraft, on the other hand, is more powerful and it can fly at 10000 meters high. It is known that the atmospheric pressure decreases with altitude to levels of 1 torr ($1/760 = 0,00131579atm$) at 150000 ft ($150000/3,281 = 45718m$) and 0.01 torr ($0.01/760 = 1,31579 \cdot 10^{-5}atm$) at 250000 ft ($250000/3,281 = 76196m$) and eventually to the highest vacuum of space. According to the Paschen's law, the equation that calculates the breakdown voltage between two electrodes in a gas as a function of gap length and pressure, the breakdown voltage decreases until a minimum value of pressure before rising again with the reduction of the pressure.

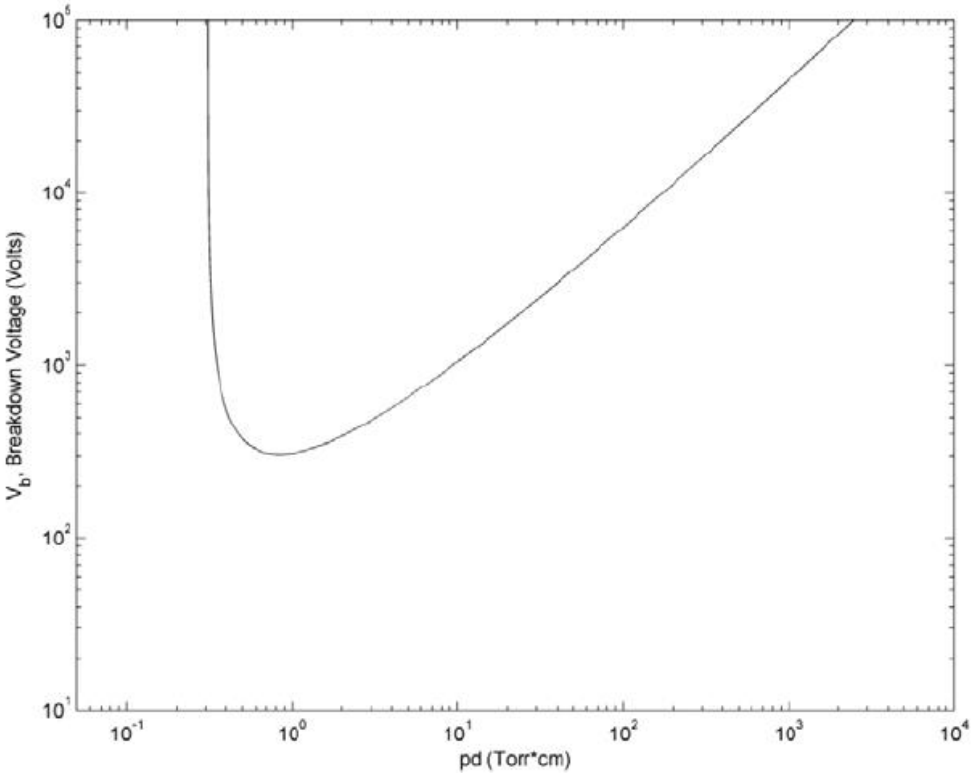

Figure 5.1: Paschen curve's trend of the air. (Source: Martins and Pinheiro 2011)

Friedrich Paschen, a German physicist, noticed that:

- With a constant gap length, the voltage necessary to arc across the gap decreased as the pressure was reduced and then increased gradually, exceeding its original value
- With a constant pressure, the voltage needed to cause an arc reduced as the gap size was reduced but only to a point. As the gap was reduced further, the voltage required to cause an arc started raising and again exceeded its original value.

This relation could be obtained also analytically by the formula:

$$V_B = \frac{B \cdot p \cdot d}{ln(A \cdot p \cdot d) - ln(ln(1 + \frac{1}{\gamma_{se}}))} \tag{5.1}$$

where:

- V_B is the breakdown voltage [V]
- **p** is the pressure [Pa]
- **d** is the gap distance [m]
- γ_{se} is the secondary-electron-emission coefficient (the number of secondary electrons produced per incident positive ion)
- **A** is the saturation ionization in the gas at a particular E/p (electric field/-pressure)
- **B** is related to the excitation and ionization energies.

The constants A and B are determined experimentally and found to be roughly constant over a restricted range of E/p for any given gas.
Assuming the insulation thickness can be converted into an air gap separation distance, it is not sufficient to prevent partial discharge between wires in the airgap, particularly in the end winding. Therefore, it is possible to calculate the fractional voltage in the airgap by following formula:

$$V_{d(frac)} = \frac{V_d}{V_d + V_i} = \frac{d \cdot \epsilon_r}{d \cdot \epsilon_r + i} \tag{5.2}$$

where:

- **d** is the air gap length
- ϵ_r is the relative permittivity of the wire insulation
- **i** is the insulation thickness

An analysis of this voltage as a function of air-gap according to Paschen's law can produce the voltage that causes the partial discharge.

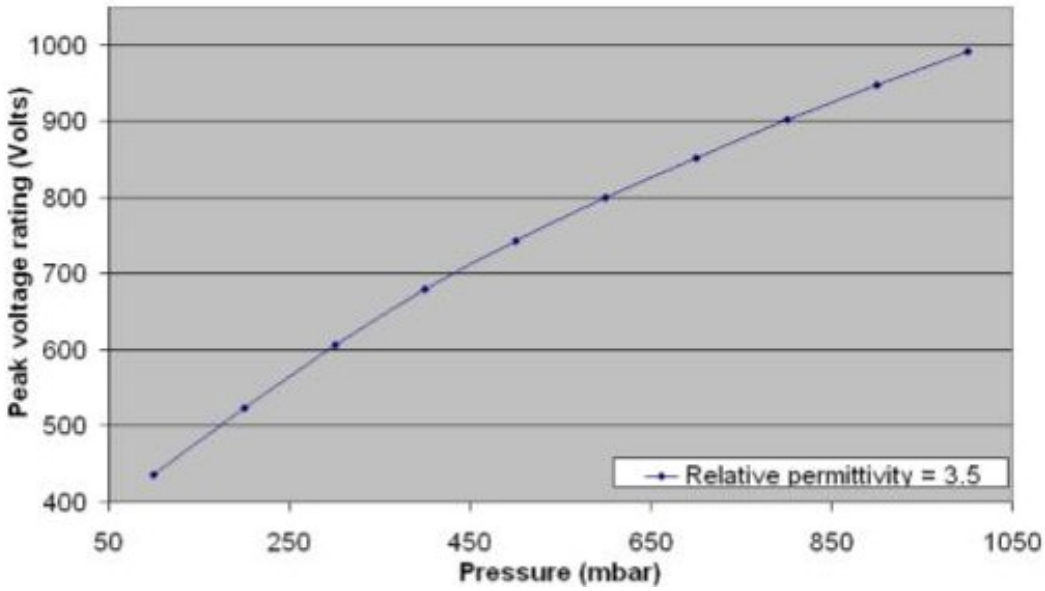

Figure 5.2: Operation of 0.04mm thick material in function of voltage breakdown and pressure. (Source: Rui and Cotton 2010)

For example here it is shown the operation of 0.04mm thick insulation (wire to wire configuration). The results show that the voltage breakdown decreases while the pressure drops.

Higher voltages are not the only challenge for the new generation of aerospace electrical machine insulation systems. The more electrical engine (MEE) aims to mount the electrical generators in a hotter part of the engine, as we said in the previous chapter, near the turbine at about $350°C$, to which is added the winding temperature. The insulation system should,therefore, withstand a peak temperature of $500°C$, but it could be higher under certain contingency situations. As the temperatures are so high the organic insulation materials now widely used are not adopted anymore. For this reason they have been replaced with inorganic material such as glass fibre, pure mica and ceramic. Due to the brittleness of these materials, they have to undergo to some constraints (winding production and its time of resistance in a harsh environment). Furthermore, the insulation layer has to be as thin as possible to save space and maximize the packing factor.

5.1 High Temperature Wire Candidates

All the wire candidates are made of nickel plated copper as the conductor material, as copper supplies high conductivity winding and nickel prevents oxidation. Wires number 1 (ceramic insulation) and 2 (mica film insulation) are commercially available while wire number 3 (insulation made of organic and inorganic material) is a prototype.

5.1.1 Ceramic Insulation

The wire number 1 characteristics are:

- 1 mm in diameter and a very thin insulation ceramic layer ($5\mu m$)
- Continuous operating temperature up to $500°C$ until peaks of $1000°C$
- Nominal operating voltage is 100 V, but it could reach also 170 V.

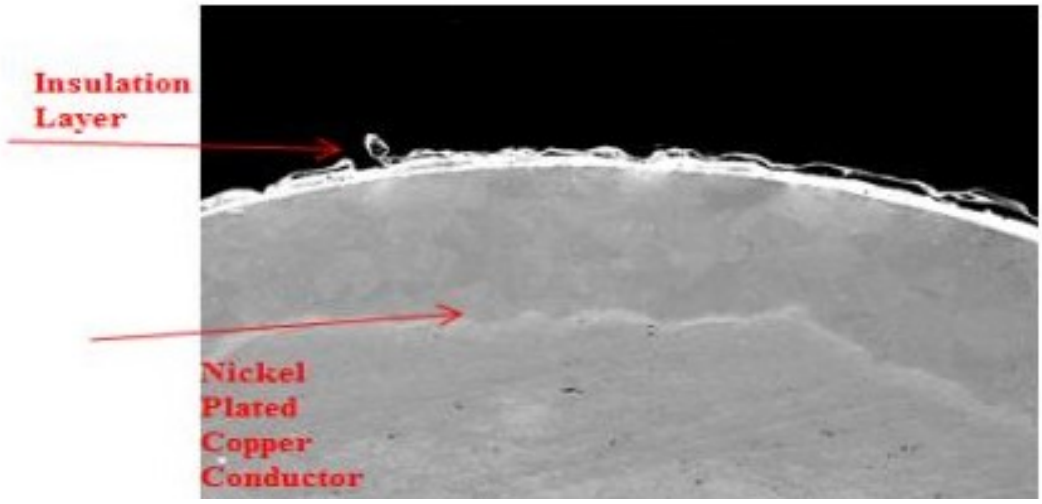

Figure 5.3: SEM scan for the ceramic insulation. (Source: Fang et al. 2013)

The SEM (Scanning Electron Microscope) scan for wire number 1 is shown in Fig. (5.3). We can clearly notice that the insulation layer is not uniform along the conductor As it is very thin, the conductor presents a large amount of area is not

covered with any insulation material at all. The solid ceramic acts as a separator between two winding wires with air supplying the actual insulation layer. Therefore, the wire is expected to perform poorly in a low pressure situation but its performance should be approximately similar to the Paschen's law curve.
No partial discharge is observed and the breakdown happens at a low voltage with a standard deviation of its voltage very low during the experimental tests.

Wire number 1	**BDV(VRMS)**	**PDIV(VRMS)**
Before thermal ageing	234.1	No PD
Standard deviation	9.45	-
After thermal ageing	233.33	No PD
Standard deviation	5.72	-

Table 5.1: Voltage result for the ceramic insulation. (Data source: Fang et al. 2013)

These results match the SEM scan. The advantage is that there is no impact of thermal cycling on the wire performance.

5.1.2 Mica film insulation

The wire number 2 presents:

- mica film as the insulation material
- fibreglass as the framework on which to carry the insulation layer
- a diameter of about 1mm
- similar working temperature of the wire number 1
- dielectric strength has to be higher than 700V.

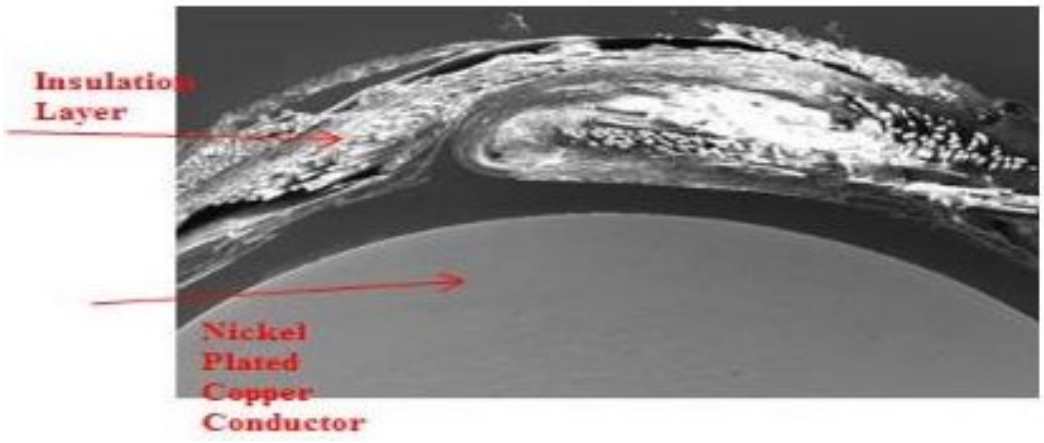

Figure 5.4: SEM scan for the mica insulation. (Source: Fang et al. 2013)

The SEM scan for wire number 2 is shown in Fig. (5.4). The insulation layer has an inhomogeneous and complex nature, therefore it is not reliable, although its thickness and its net like provides a high flexibility and delivers a high breakdown voltage. This structure involves a high standard deviation of breakdown and partial discharge inception voltage. Furthermore, the conductor and the insulation are not bonded, leaving the material free to move. This reduces the stability, unless we apply an encapsulant. An advantage of this wire is that the thermal ageing improves the stability in spite of the reduction in the wires' dielectric strength. This could be caused by the movement of mica film and fiberglass due to the thermal expansion forces.

Wire number 1	**BDV(VRMS)**	**PDIV(VRMS)**
Before thermal ageing	684.4	No PD
Standard deviation	97.70	-
After thermal ageing	502.7	430
Standard deviation	25.21	21.21

Table 5.2: Voltage result for the mica insulation. (Data source: Fang et al. 2013))

5.1.3 Prototype insulation

The wire number 3 has:

- 1.2 mm diameter
- an insulation layer assembled by both organic and inorganic materials.

Thanks to the organic part, this structure provides high flexibility before its winding and installation. After this, to remove the organic part from the layer, the wire has to undergo a curing process at high temperature. In this way, the wire is left with only a ceramic insulation that provides electrical insulation, but is not suitable for bending.

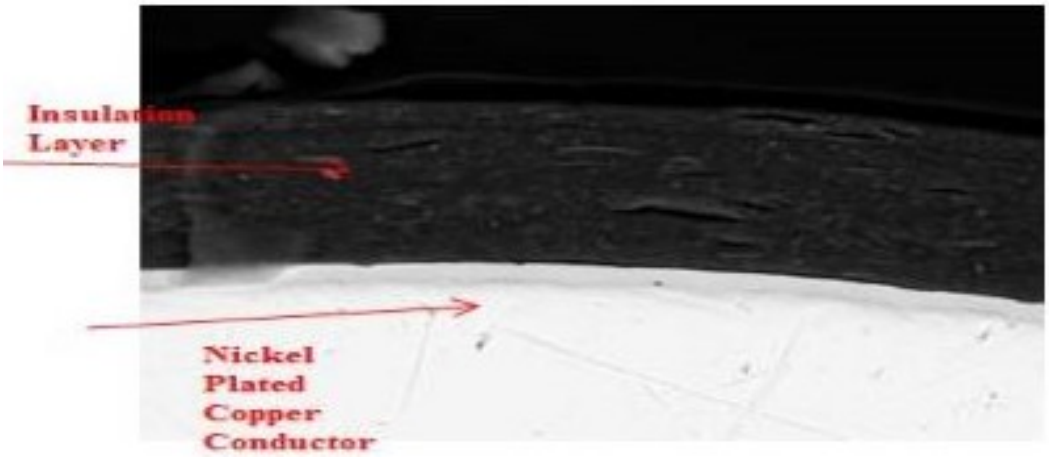

Figure 5.5: SEM scan for the prototype. (Source: Fang et al. 2013)

This is the SEM scan for wire number 3. On its conductor the insulation material is an homogeneous layer, but, due to the curing process, it later becomes uneven. This reduces its breakdown strength. Furthermore, it can be observed that partial discharge always takes place before and after the thermal ageing process.

Wire number 1	**BDV(VRMS)**	**PDIV(VRMS)**
Before thermal ageing	433.5	360
Standard deviation	36.82	18.97
After thermal ageing	346.2	260
Standard deviation	44.70	21.32

Table 5.3: Voltage result for the prototype. (Data source: Fang et al. 2013)

Chapter 6

Conclusion

The target of this thesis was to study the two possible types of motor for more electric aircraft:

- A surface-mounted permanent magnet motor with 36 slots/30 poles.
- A switched reluctance motor with 6 stator poles and 4 rotor poles.

We studied the motor through the finite element program FEMM. For the first motor, we analysed the no-load and load operation computing the flux linkage (in both operation), the no-load voltage, the cogging torque, and the torque in load operation, also mapping the MTPA point varying the direct and quadrature current. While for the switched reluctance, we considered to study only a phase of the motor calculating the three main parameters (flux linkage, co-energy and the torque).
After that, we computed the losses for each motor reporting the results always on FEMM, but in *heat flow problem* to see the trends of the temperature inside the motor.
Observing that the temperature is over 500°C, we analysed also the possible candidates for the thermal insulation. We can say that:

- Wire candidate number 1 (ceramic insulation) has evident holes in the insulation layer which make that the insulation is used only to separate the wires

resulting in low breakdown voltage and no partial discharge. The thermal withstand ability is the best one among all three candidates.

- Wire number 2 (mica insulation) presents a higher standard deviation in breakdown voltage because the mica fibre is unevenly distributed. The thermal ageing reduces its dielectric strength.

- Wire number 3 (prototype insulation) has an electrical behaviour closer to the traditional polymeric electrical wire.

It is improbable that wire 1 would meet the requirements to be used in an aerospace machine for its low levels of breakdown voltage. The other two wires show promise.

Sitography

"Il Sole 24 Ore." www.ilsole24ore.com.

"NASA." www.nasa.gov.

"CIBAS Group." www.cibas.it.

"Ministero dell'Ambiente e della tutela del territorio e del mare." www.minambiente.it.

"Aviation Coaching." www.aviationcoaching.com.

"Associazione nazionale tutela energia rinnovabili." www.anteritalia.org.

Bibliography

Al-Timimy, Ahmed et al. (2018). "Investigation of AC Copper and Iron Losses in High-Speed High-Power Density PMSM". In: *Proceedings - 2018 23rd International Conference on Electrical Machines, ICEM 2018* September, pp. 263–269.

Andriollo, M, G Martinelli, and A Morini (2003). "Macchine elettriche rotanti". In: *Cortina editore*.

Bianchi, Nicola (2001). *Calcolo delle macchine elettriche col metodo degli elementi finiti*. Cleup.

Bianchi, Nicola and Silverio Bolognani (2001). *Metodologie di progettazione delle macchine elettriche*. Cleup.

Boglietti, A et al. (2009). "The Safety Critical Electric Machines and Drives in the More Electric Aircraft : a Survey". In: *2009 35th Annual Conference of IEEE Industrial Electronics*, pp. 2587–2594.

Bolam, Robert Cameron, Yuriy Vagapov, and Alecksey Anuchin (2018). "Review of Electrically Powered Propulsion for Aircraft". In: *Proceedings - 2018 53rd International Universities Power Engineering Conference, UPEC 2018*, pp. 1–6.

Bonacina, Cesare, Alberto Cavallini, and Lino Mattarolo (1992). *Trasmissione del calore*. Cleup.

Bozhko, Serhiy et al. (2018). "Development of Aircraft Electric Starter-Generator System Based on Active Rectification Technology". In: *IEEE Transactions on Transportation Electrification* 4.4, pp. 985–996.

Cao, Wenping et al. (2012). "Overview of electric motor technologies used for more electric aircraft (MEA)". In: *IEEE Transactions on Industrial Electronics* 59.9, pp. 3523–3531.

Cavagnino, Andrea et al. (2013). "Integrated generator for more electric engine: Design and testing of a scaled-size prototype". In: *IEEE Transactions on Industry Applications* 49.5, pp. 2034–2043.

Deng, Yuhang, Simon Y. Foo, and Indranil Bhattacharya (2014). "Regenerative electric power for More Electric Aircraft". In: *Conference Proceedings - IEEE SOUTHEASTCON*, pp. 1–5.

Fang, L. et al. (2013). "Insulation performance evaluation of high temperature wire candidates for aerospace electrical machine winding application". In: *2013 IEEE Electrical Insulation Conference, EIC 2013* June, pp. 253–256.

Fujikura, The et al. (1982). "United States Patent (19)". In: 11.19.

Gallo, M. (2015). "Analisi e modellistica di un azionamento a riluttanza commutata". In:

Gao, Yi et al. (2010). "Fatigue properties of an electrical steel and design of EV/HEV IPM motor rotors for durability and efficiency". In: *SAE Technical Papers*.

Gerada, Chris and Keith J. Bradley (2008). "Integrated PM machine design for an aircraft EMA". In: *IEEE Transactions on Industrial Electronics* 55.9, pp. 3300–3306.

Giangrande, P. et al. (2018). "Design and testing of PMSM for aerospace EMA applications". In: *Proceedings: IECON 2018 - 44th Annual Conference of the IEEE Industrial Electronics Society* November, pp. 2038–2043.

Golovanov, Dmitry, Michael Galea, and Chris Gerada (2017). "High specific torque motor for propulsion system of aircraft". In: *2016 International Conference on Electrical Systems for Aircraft, Railway, Ship Propulsion and Road Vehicles and International Transportation Electrification Conference, ESARS-ITEC 2016* August 2017.

Golovanov, Dmitry et al. (2019). "A Holistic Electrical Machine Design Tool for More-Electric and Hybrid-Electric Aircraft". In: *2018 IEEE International Con-*

ference on Electrical Systems for Aircraft, Railway, Ship Propulsion and Road Vehicles and International Transportation Electrification Conference, ESARS-ITEC 2018 February 2019.

Gudmundsson, Ketill (Nov. 2019). "Design of a Magnetorheological Fluid for an Prosthetic Knee Actuator with an Optimal Geometry". In:

Gunter, Sandro et al. (2019). "Load Control for the DC Electrical Power Distribution System of the More Electric Aircraft". In: *IEEE Transactions on Power Electronics* 34.4, pp. 3937–3947.

Iosif, V et al. "Technological assessments for designing machines able to work at very high internal temperatures". In: *2016 XXII International Conference on Electrical Machines (ICEM)* (), pp. 2682–2687.

Iosif, Vadim et al. (2016). "Assessment and improvements of inorganic insulation for high temperature low voltage motors". In: *IEEE Transactions on Dielectrics and Electrical Insulation* 23.5, pp. 2534–2542.

Jumonji, S. et al. (1995). "Super heat resistant ceramic insulated wire". In: *Proceedings of the Electrical/Electronics Insulation Conference*, pp. 557–563.

Kappatou, Joya, Georgios Zalokostas, and Dimitrios Spyratos (Nov. 2016). "Design Optimization of Axial Flux Permanent Magnet (AFPM) Synchronous Machine Using 3D FEM Analysis". In: *Journal of Electromagnetic Analysis and Applications* 08, pp. 247–260.

Krishnan, Ramu (2017). *Switched reluctance motor drives: modeling, simulation, analysis, design, and applications*. CRC press.

Lusaurdi, Luca, Andrea Cavallini, and Michele Degano (2017). "The impact of impulsive voltage waveforms on the electrical insulation of actuators for more electrical aircraft (MEA)". In: *Proceedings IECON 2017 - 43rd Annual Conference of the IEEE Industrial Electronics Society* 2017-Janua, pp. 4414–4418.

Madonna, Vincenzo et al. (2019). "Thermal overload and insulation aging of short duty cycle, aerospace motors". In: *IEEE Transactions on Industrial Electronics* May, pp. 1–1.

Malec, David, Daniel Roger, and Stéphane Duchesne (2018). "An electrical machine made with inorganic rigid coils : a breakthrough toward high temperature motors designed for aeronautics". In: June, pp. 17–20.

Martins, Alexandre and Mario Pinheiro (Dec. 2011). "On the propulsive force developed by asymmetric capacitors in a vacuum". In: pp. 112–119.

Mi, Chunting, G. R. Slemon, and R. Bonert (2001). "Minimization of iron losses of permanent magnet synchronous machines". In: *ICEMS 2001 - Proceedings of the 5th International Conference on Electrical Machines and Systems* 2.1, pp. 818–823.

Miller, Timothy John Eastham (2001). *Electronic control of switched reluctance machines*. Elsevier.

Moir, Ian and Allan Seabridge (2008). *Civil Aviation Avionics*, pp. 252–256.

Quigley, Richard E. "Direct Feedback From Customers". In: *Aerospace* ().

Raymer, Daniel (2019). *Aircraft Design: A Conceptual Approach, Sixth Edition and RDSwin Student SET*.

Rosero, J. A. et al. (2007). "Moving towards a more electric aircraft". In: *IEEE Aerospace and Electronic Systems Magazine* 22.3, pp. 3–9.

Rui, Rui and Ian Cotton (2010). "Impact of low pressure aerospace environment on machine winding insulation". In: *Conference Record of IEEE International Symposium on Electrical Insulation*, pp. 1–5.

Sarlioglu, Bulent and Casey T. Morris (2015). "More Electric Aircraft: Review, Challenges, and Opportunities for Commercial Transport Aircraft". In: *IEEE Transactions on Transportation Electrification* 1.1, pp. 54–64.

Sawada, Kazuo et al. (1995). "United States Patent (19)". In: 19.

Shoujun, Song et al. (2010). "Detailed Design of a High Speed Switched Reluctance Starter/Generator for More/All Electric Aircraft". In: *Chinese Journal of Aeronautics* 23.2, pp. 216–226.

Tursini, M. et al. (2017). "A switched-reluctance motor for aerospace application: Design, analysis and results". In: *Electric Power Systems Research* 142.January, pp. 74–83.

Ullah, S. et al. (2016). "A permanent magnet assisted switched reluctance machine for more electric aircraft". In: *Proceedings - 2016 22nd International Conference on Electrical Machines, ICEM 2016*, pp. 79–85.

Villani, Marco et al. (2012). "High reliability permanent magnet brushless motor drive for aircraft application". In: *IEEE Transactions on Industrial Electronics* 59.5, pp. 2073–2081.

Wang, Shengnan et al. (2018). "Analysis of power loss of permanent magnet synchronous motors in more-electric-aircraft considering the impact of temperature". In: *IEEE/ASME International Conference on Advanced Intelligent Mechatronics, AIM* 2018-July, pp. 1184–1189.

Wang, Yinli et al. (2017). "Sensitivity analysis for performance and power density improvements in salient-pole synchronous generators". In: *Proceedings - 2017 IEEE Workshop on Electrical Machines Design, Control and Diagnosis, WEMDCD 2017* September 2018, pp. 163–168.

Weimer, Joseph A. (1993). "Electrical power technology for the more electric aircraft". In: *Proceedings of the IEEE/AIAA 12th Digital Avionics Systems Conference*, pp. 445–450.

Wheeler, Pat (2016). "Technology for the more and all electric aircraft of the future". In: *2016 IEEE International Conference on Automatica, ICA-ACCA 2016*, pp. 1–5.

Wheeler, Pat and Sergei Bozhko. "The More Electric Aircraft". In: *IEEE Electrification Magazine* 2.February 2015 (), pp. 6–12.

— (2014). "The more electric aircraft: Technology and challenges". In: *IEEE Electrification Magazine* 2.4, pp. 6–12.

Zhu, Shaohong et al. (2018). "Design Considerations of Fault-Tolerant Electromechanical Actuator Systems for More Electric Aircraft (MEA)". In: *2018 IEEE Energy Conversion Congress and Exposition, ECCE 2018* September, pp. 4607–4613.

Acknowledgements

After two long and intense years, the day is finally arrived. Writing these sentences of thanks is the final touch of my thesis. It was a period of deep learning, not just at scientific level, but also at personal one. I would like to say a few words of thanks to all the people who supported and helped during this period.

First of all, I wanted to express my gratitude to my supervisor N. Bianchi, who followed me through this path.

A special thanks to all my family, Gabriele, Marina, Valeria and Leonardo, for all the advice and directions they gave.

I would also like to thank my girlfriend, Chiara, who supported me in every sense standing always by my side.

I could not forget my personal editor Chiara, who helped me to write this LONG thesis.

Last but not least, I wanted to thank all my friends. We had always supported each other, in good times and in bad times, both during the hardship and despondency that characterized our journey in moments of joy and satisfaction to reach the goal.

A heart-felt thanks to all.

Nicolò